International Journal of Biological Macromolecules 306 (2025) 141606

Contents lists available at ScienceDirect

International Journal of Biological Macromolecules

journal homepage: www.elsevier.com/locate/ijbiomac

Hyaluronic acid-liposomes hybridized with HucMSC exosomes for enhanced exosomes transdermal delivery and acute skin photodamage repair

Yuhui Yang [a,c,1], Yong He [b,1], Hui Xing [c], Ziyi Zhao [c], Jianjin Wang [e], Shanying Li [e], Xiaosong Xu [f], Dong Ma [a,c,d,*], Yunfeng Hu [b,**]

[a] Department of Burn and Plastic Surgery, Guangzhou Red Cross Hospital, Jinan University, Guangzhou 510235, China
[b] Department of Dermatology, The First Affiliated Hospital of Jinan University, Guangzhou, Guangdong Province, China
[c] State Key Laboratory of Bioactive Molecules and Druggability Assessment, Institute of Biomedical Engineering, Jinan University, Guangzhou 510632, China
[d] MOE Key Laboratory of Tumor Molecular Biology, Jinan University, Guangzhou 510632, China
[e] Honest Medical China Co., Ltd, Zhuhai 519000, China
[f] Hengqin Perfect-Medical Laboratory Co. Ltd, Zhuhai 519000, China

ARTICLE INFO

Keywords:
Exosomes
Hyaluronic acid liposomes
Transdermal drug delivery
Anti-inflammatory

ABSTRACT

Long-term exposure to ultraviolet (UV) radiation can damage human skin, resulting in photodamage. Repairing photodamaged skin has been a major focus of research in recent years. Extensive research has shown that human umbilical cord mesenchymal stem cell-derived exosomes (Exo) possess anti-inflammatory, pro-angiogenic, and wound healing properties, holding great potential for treating skin damage. However, due to the limitations of exosomes alone, such as poor transdermal penetration, instability, and low utilization, there is an urgent need for new delivery strategies. We designed a hybrid nanovesicle (HL@Exo) by combining ultrasonic incubation with membrane extrusion to fuse Exo with HL. HL@Exo capitalizes on the advantages of liposomal carriers and the permeation-enhancing properties of hyaluronic acid to effectively facilitate transdermal delivery of Exo. The successful fusion of HL@Exo and its skin penetration were verified by methods such as fluorescent labeling, western blotting, Transwell assays, and *in vivo* imaging. *In vitro* studies on photodamaged keratinocytes and endothelial cells demonstrated HL@Exo ability to promote cell proliferation, repair, angiogenesis, and reduce inflammation. In a laser-induced skin photodamage model, HL@Exo enhanced collagen regeneration, accelerated wound healing, and demonstrated significant anti-inflammatory effects, indicating its potential as a non-invasive treatment and offering a novel strategy for the clinical application of Exo.

1. Introduction

Ultraviolet radiation has various harmful effects on human skin, manifesting as pathological changes such as sunburn, erythema and edema, which further lead to photodamage. Photodamage caused by ultraviolet radiation is currently one of the most common causes of skin damage and severely affecting people's quality of life [1–4]. Human umbilical cord mesenchymal stem cell-derived exosomes are rich in various bioactive components, including specific DNA, microRNA, proteins, and other active molecules. Among them, miRNAs can target and regulate ROS-related genes (*e.g.*, SOD, CAT) to alleviate oxidative stress; protein components can activate the Wnt/β-catenin pathway, promoting cell migration, proliferation, angiogenesis, collagen synthesis, and skin tissue repair. Additionally, TGF-β1 and HSP70 in exosomes can modulate the immune microenvironment, facilitating the repair of the damaged tissue microenvironment. These components collectively endow exosomes with properties such as immune modulation, wound healing promotion, and anti-inflammatory effects, making them widely used in drug delivery, tissue repair, and regeneration [5]. For example, Yin et al. demonstrated that exosomes derived from human umbilical

* Correspondence to: D. Ma, State Key Laboratory of Bioactive Molecules and Druggability Assessment, Institute of Biomedical Engineering, Jinan University, Guangzhou 510632, China.
** Corresponding author.
E-mail addresses: tmadong@jnu.edu.cn (D. Ma), huyunfeng@jnu.edu.cn (Y. Hu).
[1] Y.Y. and H.Y. contributed equally to this work.

https://doi.org/10.1016/j.ijbiomac.2025.141606
Received 9 October 2024; Received in revised form 13 February 2025; Accepted 27 February 2025
Available online 28 February 2025

cord mesenchymal stem cells (UCB-Exo) promote wound healing and reduce scar formation by utilizing Spry1 and PTEN [6,7]. Zhang et al. developed an exosome hydrogel that alleviated early inflammatory responses and promoted healing in damaged skin [8]. The stratum corneum of human skin serves as a natural barrier, effectively preventing the penetration of molecules and particles. Additionally, when exosomes are directly applied to the skin surface, they are prone to degradation by enzymes in the skin microenvironment, which can lead to their loss of activity. Exosomes are also highly sensitive to environmental factors such as heat and ultraviolet (UV) radiation, further compromising their stability and bioavailability. Relying solely on diffusion mechanisms makes it difficult to achieve effective utilization. As a result, invasive treatments are often employed. However, invasive treatments are prone to causing secondary damage to the damaged skin and are rapidly cleared, limiting their therapeutic functions. On the other hand, chronic skin damage, such as UV-induced skin aging and burn wounds, requires a relatively long recovery time. Single exosomes face inherent limitations in terms of permeability, stability, and functional specificity. Therefore, the design of exosome-based materials that combine multifunctionality with high efficiency is a key focus of current research.

Transdermal drug delivery systems are lauded as one of the most promising non-invasive drug delivery methods due to their avoidance of first-pass effects, non-invasiveness, and high efficiency [9]. Liposomes, as carriers, offer high biocompatibility, low toxicity, and high encapsulation efficiency, making them widely applicable in transdermal delivery [10]. For instance, Malakar et al. developed liposomal gels containing insulin for treating insulin-dependent diabetes, achieving favorable outcomes, Kurakula et al. loaded lipid nanoparticles and avanafil into hydrogel films for transdermal treatment of erectile dysfunction, significantly improving drug solubility and bioavailability [11,12]. Hyaluronic acid (HA), as a penetration enhancer, can increase the water content of the stratum corneum and form complexes with skin phospholipids to open channels for enhanced penetration. For example, Manca et al. formulated HA vesicles using hydrophilic curcumin and hyaluronic acid sodium, demonstrating that HA can promote rapid drug deposition in the skin, beneficial for inflammation prevention and wound healing [13]. Wang et al. grafted cyclodextrin onto HA to form polymeric micelles for treating atopic dermatitis, showing enhanced drug penetration and prolonged retention in the skin [14]. Therefore, leveraging the carrier advantages of liposomes and the penetration-enhancing properties of hyaluronic acid offers a new approach for the non-invasive delivery of exosomes in the skin.

Building on the above discussions, this study utilized ultrasonic incubation combined with membrane extrusion to hybridize HL with Exo, designing a hybrid nanovesicle (HL@Exo) with efficient delivery and therapeutic functions. We developed HL@Exo, a hybrid nanovesicle that incorporates hyaluronic acid (HA), a permeation-enhancing molecule, into conventional liposomes. This design reduces the resistance of the stratum corneum barrier, enhances the rapid deposition of exosomes in the skin, and increases their mobility, thereby significantly improving their efficiency in penetrating the stratum corneum. Additionally, the bilayer membrane structure of HA liposomes provides protection and controlled-release functionality for exosomes, thereby improving their stability and utilization efficiency. Mechanistically, HL@Exo exhibits remarkable synergistic effects. On one hand, HL@Exo increases superoxide dismutase (SOD) activity and decreases the production of malondialdehyde (MDA), thereby mitigating oxidative stress-induced damage to DNA and proteins and suppressing the excessive production of inflammatory mediators. On the other hand, HL@Exo directly downregulates pro-inflammatory factors, modulating immune balance in the damaged area and restoring the normal immune microenvironment of skin tissues. Furthermore, HL@Exo promotes the repair of the epidermal barrier, facilitates the orderly arrangement of collagen fibers, and regulates cell proliferation and apoptosis, collectively accelerating the regeneration and structural restoration of skin tissues. This dual anti-inflammatory and antioxidant mechanism not only enables HL@Exo to achieve non-invasive treatment of acute photodamaged skin but also provides a novel strategy for advancing the clinical application of exosome-based therapies (Scheme 1).

2. Materials and methods

2.1. Materials preparation

Soy lecithin was purchased from Aladdin Biochemical Technology Co., Ltd. (Shanghai, China). Cholesterol (Cho) was purchased from Qiyun Biotechnology Co., Ltd. (Guangzhou, China). Sodium hyaluronate was purchased from JinSui Biotechnology Co., Ltd. (Shanghai, China). PKH26 and PKH67 fluorescent kits were purchased from Sigma-Aldrich. Absolute ethanol (AR) was purchased from Guangzhou Chemical Reagent Factory. DMEM, trypsin, fetal bovine serum, and penicillin-streptomycin double antibody were purchased from Gibco (USA). CCK-8 kit, CAT kit, SOD kit, and MDA kit were purchased from Beyotime Biotechnology Co., Ltd. (Shanghai, China). Mouse anti-KI67, IL-6, IL-1β, and TNF-α antibodies were purchased from Servicebio Technology Co., Ltd. (Wuhan, China). Exo were from Hengqin Perfect-Medical Laboratory Co. Ltd. Human umbilical vein endothelial cells (HUVECs) and immortalized human keratinocytes (HaCat) were purchased from Meisen Cell Technology Co., Ltd. (Zhejiang, China).

2.2. Research on the preparation process of hyaluronic acid liposome exosomes (HL@Exo)

2.2.1. Preparation of hyaluronic acid liposomes (HL)

HL was prepared using a combination of reverse-phase evaporation, high-speed homogenization, and microfluidization, based on detailed methods previously described [10]. Briefly, soy lecithin and cholesterol in a 30:1 (*w*/w) ratio were added to 30 mL absolute ethanol, completely dissolved by water bath heating, and stirred for 2 h for thorough mixing. Concurrently, HA powder (0.1 %, *w/v*) with a molecular weight of 1–1.5 M was accurately weighed and dissolved in phosphate-buffered saline (PBS, pH = 7.4) by stirring for 4 h to obtain the HA solution. Under magnetic stirring, the two solutions were slowly mixed, and the mixture was dispersed and emulsified using a high-shear dispersing emulsifier to form a stable W/O emulsion. Finally, rotary evaporation, PBS hydration, and microfluidization were used to obtain HL [15].

2.2.2. Preparation of hybrid hyaluronic acid liposome exosomes (HL@Exo)

Considering previous studies and coupling efficiency, this study employed ultrasonic incubation combined with membrane extrusion to prepare HL@Exo. Briefly, 1 mg Exo (0.540 mg protein content) was dissolved in 1 mL HL, mixed thoroughly by vortexing and ultrasonic treatment (30 % maximum amplitude, 5-s pulse on/off, 3 min), and then incubated in a 37 °C shaker for 1 h. The mixture was then passed through 400 nm and 200 nm polycarbonate membranes, manually pushed back and forth 30 times, resulting in stable HL@Exo [16–18].

2.2.3. Fluorescent labeling of hybrid hyaluronic acid liposome exosomes (HL@Exo)

Fluorescent labeling was used to separately label the liposomes and exosomes in HL@Exo [19]. According to the dye kit instructions, 50 μL PKH-26 dye working solution was added to 200 μg exosome solution, and 5 μL PKH-67 dye working solution was added to 100 μL hyaluronic acid liposome solution. Both were vortexed and incubated at room temperature for 10 min. The solutions were centrifuged at 4 °C to remove excess dye, and the precipitate was resuspended in PBS (pH = 7.4) to obtain fluorescently labeled exosomes dye complexes and hyaluronic acid liposome dye complexes. The fluorescently labeled HL@Exo was prepared using the same method, avoiding light throughout the process. Three parallel controls were set for each group.

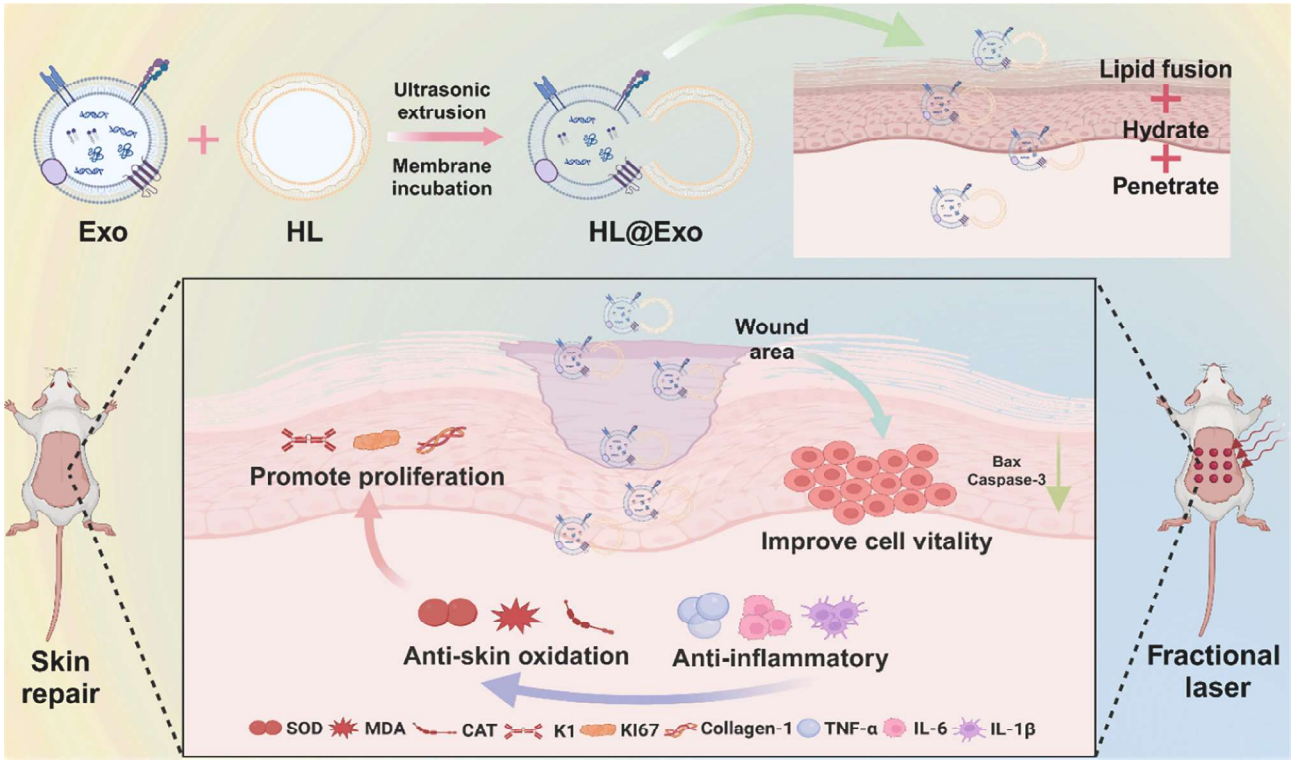

Scheme 1. Design and treatment illustration of HL@Exo transdermal delivery system for acute skin photodamage.

2.2.4. Characterization

The particle size, zeta potential, and PDI of HL, Exo, and HL@Exo were measured using a nanoparticle size analyzer (Malvern). The hydrodynamic diameter distribution of HL, Exo, and HL@Exo was analyzed using a nanoparticle tracking analyzer (NTA) [20]. Structural characterization of PKH-26 labeled Exo and PKH-67 labeled HL was performed using a laser scanning confocal microscope (LSM 880). The morphology of HL, Exo, and HL@Exo was observed using a field emission cryo-transmission electron microscope (Cryo-FE-TEM) with a working voltage of 200 kV (one set of samples was negatively stained with 1 % phosphotungstic acid, while another set was unstained for elemental composition and distribution analysis) [21]. Western blotting was used to verify the expression of CD63, TSG101, CD81, and CD9 in Exo and HL@Exo, and detection was performed using a chemiluminescence imaging system after incubation.

2.3. Skin pharmacokinetic analysis of HL@Exo

2.3.1. Quantitative analysis of in vitro simulated skin penetration

A Franz diffusion cell with a diffusion area of 1.767 cm^2 was used to conduct *in vitro* simulated skin penetration experiments on Exo and HL@Exo labeled with the specific dye PKH-26 [22]. PBS (pH = 7.4) was filled in the receiving chamber and continuously stirred at 200 rpm/min, maintaining the diffusion cell temperature at 37 °C using a circulating water bath. Suitable-sized mouse skin was clamped between the donor and receiver chambers, exposing the dermis to PBS (pH = 7.4). Freshly prepared PKH-26 labeled Exo and HL@Exo sample solutions (both at 0.1 % Exo concentration) were applied to the stratum corneum in the donor chamber. At different time points (1 h, 3 h, 5 h, 7 h), 1 mL samples were taken from the receiver chamber through the sampling port and replaced with equal volumes of PBS (pH = 7.4). The exosome content in the samples was analyzed by measuring the fluorescence intensity at 551 nm using a multifunctional microplate reader (Synergy H1) [23]. Three parallel controls were set up in each group.

2.3.2. Analysis of skin penetration depth and distribution

After the above *in vitro* penetration experiment using the Franz diffusion cell for 7 h, excess sample solution was removed from the skin surface. The skin was extracted from the diffusion cell, washed with physiological saline to ensure no residual sample, dried with filter paper, and cut into approximately 1 cm^2 sections. The skin sections were embedded in OTC compound, fixed with liquid nitrogen, and vertically sliced into 10 μm thick sections using a cryostat at −20 °C. The skin sections were mounted on slides and the fluorescent distribution in the skin was observed using an advanced inverted fluorescence microscope (AxioCamMRc), selecting a filter with an emission wavelength of 567 nm and an excitation wavelength of 551 nm.

2.3.3. In vivo penetration experiment

To determine the effect of HL on the transdermal penetration and retention of Exo, *in vivo* imaging was used on mice. Briefly, after anesthetizing the mice, the hair on both legs was removed using a shaver and depilatory cream to eliminate interference with fluorescence imaging. Then, 20 μL of PKH-26-labeled Exo and HL@Exo suspension (both at 0.1 % Exo concentration) was evenly applied to the left and right legs of each mouse, respectively (left leg for Exo, right leg for HL@Exo) to simulate the transdermal effects of the two materials on living animals. After 2 h, the mice were euthanized, and the thigh skin tissues were removed. The distribution of fluorescence in the underlying muscle tissue was observed using a small animal *in vivo* imaging system (FX Pro) to determine whether the exosomes penetrated the skin. Additionally, the proportion of fluorescence that passed through was quantified by fluorescence analysis. The excised skin tissue was frozen and vertically sectioned to produce skin slices that were mounted on slides and observed for exosome distribution using an advanced inverted fluorescence microscope (DMi8) [24]. Three parallel controls were set up for each group. The results were expressed as mean value and standard deviation.

2.3.4. In vitro cell penetration experiment

A Transwell system with human keratinocytes (HaCat) was established as an *in vitro* tissue model. Briefly, 1×10^6 HaCat cells were seeded in the upper chamber of the Transwell system and cultured at 37 °C, 5 % CO_2 until the cells adhered completely. Another 1×10^6 cells were seeded in the lower chamber to allow cell adhesion. In the upper chamber, 200 μL of fluorescently labeled Exo and HL@Exo were added and incubated. After 12 h, the cells in the lower chamber were washed several times with cold PBS and stained with Hoechst. After incubation, the lower chamber cells were washed and observed using confocal laser scanning microscopy (CLSM) [25]. Three parallel controls were set up in each group. Fluorescence intensity was measured using ImageJ 5.0 software and quantitatively analyzed.

2.4. Effects of HL@Exo on HaCat and HUVECs

2.4.1. Establishment of a photodamaged HaCat cell model

Human keratinocytes (HaCaT) were cultured in DMEM medium supplemented with 10 % fetal bovine serum and 1 % antibiotics at 37 °C, 5 % CO_2 for 24 h. The medium was removed, and the cells were covered with a thin layer of PBS. The cells were then irradiated with an ULTRAVITALUX lamp placed 10 cm from the cells at an energy level of 100 mJ/cm^2 [26]. Three parallel controls were set up in each group.

2.4.2. Effect of HL@Exo on the viability of photodamaged HaCat cells

HaCaT cells were seeded in 96-well plates at a density of 5×10^3 cells per well. After irradiation, the cells were treated with equal concentrations of HL, Exo, and HL@Exo (0.1 % Exo concentration). The control group was cultured in medium only. After 24 h, cell viability was measured using the CCK8 assay. The materials were removed, and CCK-8 reagent was added to each well. After 2 h of incubation, the absorbance at 450 nm was recorded using a multifunctional microplate reader to calculate the cell proliferation rate for each treatment. Three parallel controls were set up for each group. The results were expressed as mean value and standard deviation.

2.4.3. Simulated wound healing experiment

First, HaCaT cells were seeded in 6-well plates at a density of 2×10^5 cells per well. After the cells adhered completely, a photodamaged model was established, and a scratch was made in the center of each well using a 200 μL sterile pipette tip. The cells were washed twice with PBS (pH = 7.4) and cultured in serum-free DMEM containing HL, Exo, and HL@Exo (0.1 % Exo concentration). The control group was cultured in medium only. The cell migration was observed and recorded under a microscope at 0 h, 12 h, and 24 h. The scratch width in the images was quantified using ImageJ software to calculate the healing rate. Three parallel controls were set up for each group. The results were expressed as mean value and standard deviation.

2.4.4. Protective effect of HL@Exo on photodamaged HaCat cells

HaCat cells were seeded in 24-well plates at a density of 5×10^4 cells per well and cultured overnight to allow cell adhesion. The old medium was removed, and the cells were treated with complete medium containing different materials (HL, Exo, and HL@Exo, 0.1 % Exo concentration). After 24 h of incubation, live-dead cell staining was performed using a kit, and the cells were observed and photographed using an inverted fluorescence microscope. Three parallel controls were set up in each group.

2.4.5. Real-time quantitative PCR (qRT-PCR) analysis of HaCat apoptosis

The potential mechanism of HL@Exo in inhibiting HaCat apoptosis was investigated using qRT-PCR. Briefly, HaCat cells were seeded in 24-well plates at a density of 5×10^4 cells per well. After irradiation, the cells were treated with equal concentrations of HL, Exo, and HL@Exo (0.1 % Exo concentration). The control group was cultured in medium only. After 24 h of incubation, the sample solutions were removed, total RNA was extracted from the cells, and reverse transcription was performed according to the kit instructions. Finally, the expression of Caspase-3, Bcl-2, and Bax in the cells was measured using a real-time fluorescence quantitative PCR instrument [27]. The primer sequences used in this study are listed in Table S1. Three parallel controls were set up for each group. The results were expressed as mean value and standard deviation.

2.4.6. Study on antioxidant properties of photodamaged HaCat cells

HaCat cells were seeded in 24-well plates at a density of 5×10^4 cells per well. After irradiation, the cells were treated with equal concentrations of HL, Exo, and HL@Exo (0.1 % Exo concentration). The control group was cultured in medium only. After 24 h of treatment, cell suspensions were collected. To assess the oxidative damage in UV-damaged HaCaT cells, we measured the levels of intracellular SOD, CAT, and MDA. According to the manufacturer's instructions, the enzyme activities of SOD, MDA, and CAT were measured using assay kits [28]. To explore the protective mechanism of HL@Exo against UV-induced damage in HaCaT cells, we employed immunofluorescence to assess the expression level of the DNA double-strand break marker γH2AX. The expression of IGF-1 and γH2Ax in the cells was measured using immunofluorescence staining. Three parallel controls were set up for each group. The results were expressed as mean value and standard deviation.

2.4.7. HUVECs proliferation experiment

HUVECs were seeded in 96-well plates at a density of 5×10^3 cells per well and incubated at 37 °C, 5 % CO_2 for 24 h. The medium was removed, and the cells were treated with culture medium containing HL, Exo, and HL@Exo (0.1 % Exo concentration). The control group was cultured in medium only. After 24 h, CCK-8 reagent was added to the experimental and blank wells. After 2 h of incubation in the dark, the optical density at 450 nm was measured using a microplate reader to calculate the cell proliferation rate for each treatment. Three parallel controls were set up for each group. The results were expressed as mean value and standard deviation.

2.4.8. HUVECs migration experiment

HUVECs were seeded in 6-well plates at a density of 2×10^5 cells per well. Once the cells adhered, a scratch was made in the center of each well using a 200 μL sterile pipette tip. The cells were washed twice with PBS (pH = 7.4) and cultured in serum-free DMEM containing HL, Exo, and HL@Exo (0.1 % Exo concentration). The control group was cultured in medium only. Cell migration was observed and recorded under a microscope at 0 h, 12 h, and 24 h. The scratch width in the images was quantified using ImageJ software to calculate the healing rate. Three parallel controls were set up for each group. The results were expressed as mean value and standard deviation.

2.4.9. Endothelial tube formation assay

HUVECs were cultured with Exo, HL, and HL@Exo (all at 0.1 % Exo concentration) for 48 h. The control group was cultured in medium only. Matrigel (200 μL) was plated in 12-well plates and incubated at 37 °C for 15 min to solidify. Treated cells were then seeded onto the solidified Matrigel at 5×10^5 cells per well. After 8 h of incubation, tube formation was observed under a microscope, and the number of tubes formed was quantified using ImageJ software [29]. Three parallel controls were set up in each group.

2.5. Application in treatment of acute photodamage animal model

2.5.1. Establishment of fractional laser-induced acute skin injury

Twenty-five female BALB/C mice (6–8 weeks old, average weight 18 g) were purchased from Beijing Vital River Laboratory Animal Technology Co., Ltd. (Beijing, China). All mice were housed in an SPF-grade laboratory, with daily changes of bedding, water, and feed. The housing conditions were maintained at a temperature of 22–24 °C, relative

humidity of 60 %, with a 12-h light/dark cycle. Mice were acclimatized to the experimental environment for one week before the experiment. All animal experiments complied with the regulations of the Animal Use and Management Committee of Jinan University and were approved by the Ethics Committee (Ethics No. IACUC-20231023-07). The modeling method simulated human skin fractional laser. Mice were anesthetized and depilated using a depilatory cream. Twenty-four hours after depilation, the depilated area was evenly scanned with a CO_2 fractional laser instrument (Koyolaser) to induce an acute skin photodamage model in mice. The laser energy was 2.5 mJ/g, with a 10 × 15 mm lattice range, repeated once. Successful modeling was indicated by the appearance of red spots or slight exudate on the back skin of the mice.

2.5.2. Kinetics of exosome penetration in photodamaged skin

To explore the effective utilization of Exo during the treatment process, dynamic analysis of Exo penetration was conducted through fluorescence labeling and live imaging. PKH-26-labeled Exo and HL@Exo were used to trace the penetration of exosomes through photodamaged skin. The modeling method was as described above. After 12 h of treatment, mice were euthanized, and the back skin was collected. At 0 h and 12 h, the penetration of exosomes was observed using an *in vivo* imaging system and quantified by fluorescence analysis. To avoid fluorescence quenching, the entire process was conducted in the dark. Skin tissues were fixed with 4 % (*w/v*) paraformaldehyde and sectioned for observation of fluorescently labeled exosomes in the tissue using a fluorescence microscope [30]. Three parallel controls were set up in each group.

2.5.3. Skin repair and histological evaluation in mice

After successful modeling of acute laser-induced skin injury in mice, the mice were randomly divided into five groups, each consisting of 5 mice: the healthy group, model group (PBS), Exosome (Exo) group, Hyaluronic Liposomes (HL) group, and hybrid Hyaluronic Acid Liposome Exosomes (HL@Exo) group. The healthy group received no treatment (blank control), while on the first day post-modeling, the model group received phosphate-buffered saline (PBS), and the Exo group, HL group, and HL@Exo group started treatment, which continued for 7 days. The healing of the dorsal wounds of the mice was tracked and photographed on days 1, 3, 5, and 7 post-injury. Local observations were conducted using a dermatoscope, and detailed records of mouse body weight and dorsal skin injury changes were maintained. At the end of the experiment, dorsal skin tissue samples from each group of mice were collected and fixed in 4 % paraformaldehyde solution. The tissue samples were then dehydrated, embedded in paraffin, and sectioned into 4 μm thickness. Histological changes in the skin were observed using H&E, Masson's trichrome, and immunohistochemical staining. Additionally, Image J software was used to measure the epidermal thickness, collagen volume fraction, and expression levels of relevant proteins in the skin of each group. The epidermal thickness, collagen volume fraction, or protein expression intensity of each sample was calculated as the average of three random sites within the sample [30].

2.5.4. Enzyme-linked immunosorbent assay (ELISA) of mouse skin tissue

The sandwich enzyme-linked immunosorbent assay (ELISA) technique was employed following the protocol provided by the manufacturer of the assay kit. Specific antibodies against mouse IL-6, IL-1β, TNF-α, SOD, and MDA were precoated onto high-affinity enzyme immunoassay plates. Standard samples, test samples, and biotinylated detection antibodies were added to the wells of the enzyme immunoassay plate. After incubation, IL-6, IL-1β, TNF-α, SOD, and MDA present in the samples bound to the solid-phase antibodies and detection antibodies. Unbound substances were removed by washing, and horseradish peroxidase-labeled streptavidin was added. After washing, TMB chromogenic substrate was added, and the plate was shielded from light during color development. The intensity of the color reaction was directly proportional to the concentration of the analytes in the sample. The reaction was terminated by adding a stop solution, and absorbance values were determined at specific wavelengths.

2.5.5. Immunofluorescence staining of mouse skin tissue

To explore the specific role of HL@Exo in cell proliferation and apoptosis regulation, we examined the expression levels of Ki67、VEGF, and PCNA. After treatment, the skin tissues from each group were embedded in paraffin and sectioned. Antigen retrieval was performed, followed by blocking in mouse serum for 30 min. Subsequently, the sections were treated with primary and secondary antibodies and then incubated overnight at 4 °C. Cell nuclei were counterstained with 4,6-diamidino-2-phenylindole (DAPI). Fluorescence characteristics were observed using an M165 FC fluorescence microscope (Leica), and fluorescence intensity was measured and quantitatively analyzed using Image J 5.0 software.

2.5.6. Terminal Deoxynucleotidyl transferase dUTP Nick-end labeling (TUNEL) staining

To evaluate cell apoptosis in skin tissues following acute photodamage, we assessed the expression levels of TUNEL in the skin tissues. Fluorescein-labeled dUTP was incorporated into the 3′-ends of DNA, allowing the observation of apoptotic cells under a fluorescence microscope. TUNEL staining kits were used to detect apoptosis in paraffin-embedded skin sections, and apoptotic cells in the epidermis were observed using a fluorescence microscope.

2.6. Biocompatibility analysis

2.6.1. Skin sensitization test

To assess the irritation and sensitization of the materials on mouse skin, a continuous three-day application was performed on the back skin of the mice. Observations of peeling, scabbing, and edema at the application sites were recorded using a dermatoscope.

2.6.2. In vivo toxicity

After completion of the therapeutic interventions, euthanasia was performed on the mice from each experimental group. The heart, liver, spleen, lungs, and kidneys were excised and washed repeatedly with phosphate-buffered saline (pH = 7.4) to remove blood stains. Subsequently, the tissues were immersed in a 4 % (*w/v*) paraformaldehyde solution, followed by paraffin embedding, sectioning, and H&E staining. Observation and photography were conducted using an upright microscope (Motic). Simultaneously, blood was collected *via* eyeball extraction, and serum was obtained by centrifugation. The serum was promptly frozen in liquid nitrogen and stored at −80 °C for subsequent biochemical analysis.

2.7. Statistical analysis

All data were presented as mean ± standard deviation (SD). Differences between different experimental groups were analyzed using the One-way ANOVA method in GraphPad software (Inc., LA Jolla, CA, USA). Significance was determined based on the P value, where $^{*}P < 0.05$; $^{**}P < 0.01$; $^{***}P < 0.001$; $^{****}P < 0.0001$.

3. Results and discussions

3.1. Preparation and characterization of hybrid hyaluronic acid liposome exosomes (HL@Exo)

In this study, hyaluronic acid liposome-exosome hybrid vesicles (HL@Exo) were successfully fabricated using an ultrasound-assisted incubation method combined with membrane extrusion technology. The resulting hybrid vesicles were subjected to comprehensive characterization from multiple perspectives. Initially, the morphology of Exo,

HL, and HL@Exo was observed using Cryo-Field Emission Transmission Electron Microscope, as depicted in Fig. 1b. Exo exhibited typical spherical vesicular structures, while HL showed uniform distribution and increased particle size. During the membrane extrusion process, the lipid membrane of Exo deformed and successfully hybridized with HL [19]. For visual confirmation of their fusion, Exo labeled with PKH-26 (red) and HL labeled with PKH-67 (green) were characterized using laser scanning confocal microscopy (LSM 880), as shown in Fig. 1c. HL@Exo exhibited a yellow color post-hybridization, validating the successful fusion. The particle size and zeta potential of liposomes are critical factors influencing their transdermal penetration through the skin. Studies have shown that liposomes with a particle size smaller than 500 nm can more effectively penetrate the skin [32]. Nanometer-sized particles enhance both their permeability and the enhanced permeability and retention (EPR) effect. Zeta potential is a parameter that measures the mobility of charged particles in a solution, which is influenced by the charge and size of the particles. As shown in Fig. 1d, compared to Exo, HL@Exo has a larger absolute zeta potential. A higher absolute zeta potential indicates that the charged particles in the dispersion system are more uniformly dispersed in the solvent, making them less prone to aggregation or precipitation [33]. The stable zeta potential provides HL@Exo with improved physical stability, reducing the risk of degradation of Exo. Additionally, the well-dispersed particles can prolong their residence time on the skin surface, increasing the effective concentration of HL@Exo in the skin tissue. Moreover, the negative surface charge can form a stable hydration layer with water molecules, improving the wettability and diffusivity of the dispersion system, which aids in transdermal drug delivery. Furthermore, particle size and zeta potential analysis using a Malvern particle size analyzer revealed that Exo, HL, and HL@Exo had particle sizes and zeta potentials of 126.4 ± 2.33 nm (−11 ± 0.17 mV), 169.98 ± 3.46 nm (−22.5 ± 0.33 mV), and 234.22 ± 3.07 nm (−17.21 ± 0.25 mV), respectively, as shown in Fig. 1(d, e). Compared to Exo, HL@Exo exhibited a decreased zeta potential post-membrane extrusion due to the insertion of membrane lipids, indicating successful hybridization between hyaluronic acid liposomes and exosomes [34]. Protein imprinting analysis confirmed the presence of exosome marker proteins CD9, CD63, CD81, and TSG101 in HL@Exo, as shown in Fig. 1f, demonstrating that this preparation technique adequately preserves exosome activity without affecting their efficacy [35]. NTA analysis of Exo, HL, and HL@Exo revealed that their particle sizes followed a Gaussian distribution, as shown in Fig. S1. The hydrodynamic diameters were approximately 166 ± 9.1 nm for Exo, 223.0 ± 5.1 nm for HL, and 277.6 ± 12.7 nm for HL@Exo (Fig. S1a). These results indicate that the hybrid vesicles HL@Exo, successfully fabricated through ultrasonic incubation and membrane extrusion techniques, possess relatively small hydrodynamic diameters, which suggests their potential for effective skin penetration and controlled release of active substances. These findings are consistent with the results obtained using the Malvern Zetasizer. Additionally, cryo-transmission electron microscopy (cryo-TEM) was employed to characterize the morphology of non-stained Exo, HL, and HL@Exo. The analysis confirmed that Exo, HL, and HL@Exo retained intact, near-spherical structures, consistent with the phosphotungstic acid-stained TEM images shown in Fig. 1b. No significant morphological changes were observed. The non-stained HL (Fig. S1c) and HL@Exo (Fig. 1g) exhibited distinct phospholipid bilayers. Compared with the classical spherical morphology of exosomes, some hybrid vesicles showed irregular vesicular structures. Furthermore, Elemental composition and distribution analysis (EDS) confirmed the vesicular nature of the particles by detecting the presence of elements C, N, O, and P in Exo, HL, and HL@Exo (Figs. 1g and S1c) [36]. To evaluate the stability of Exo, HL, and HL@Exo, their particle size and polydispersity index (PDI) were continuously monitored over seven days under storage conditions at 4 °C, as shown in Fig. S1. Although all three exhibited varying degrees of

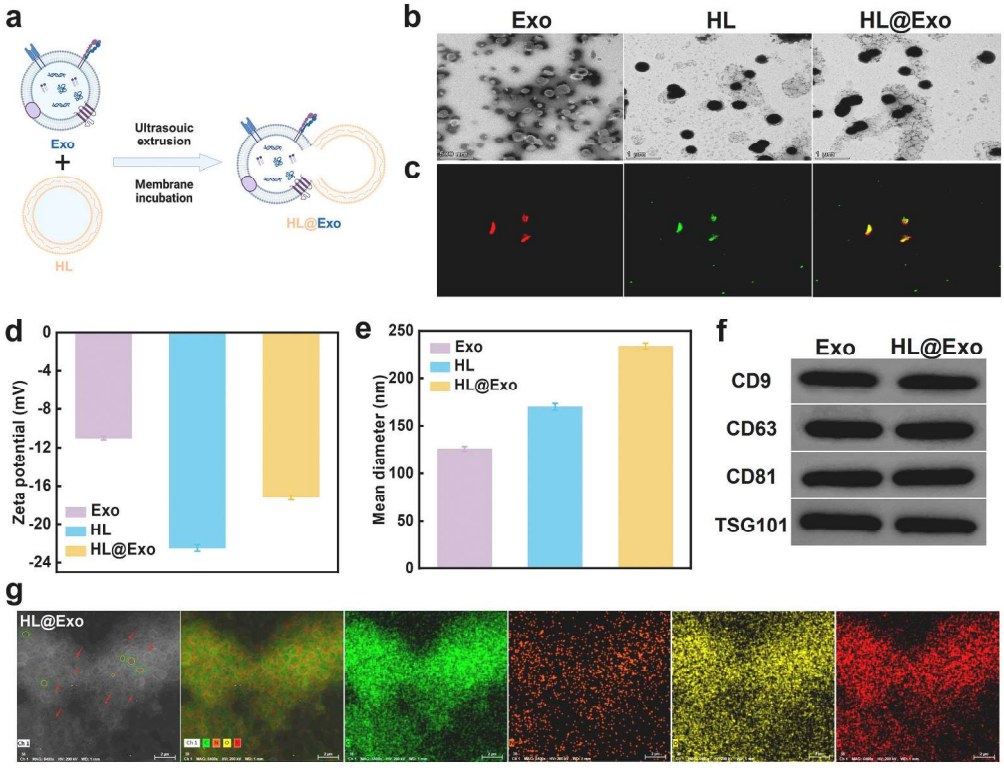

Fig. 1. Synthesis and characterization of HL@Exo. (a) Schematic of HL@Exo synthesis. (b) Cryo-TEM images of Exo, HL, and HL@Exo (phosphotungstic acid negative staining). scale bars = 500 nm, 1 μm, and 1 μm, respectively. (c) Confocal fluorescence microscopy images of Exo, HL, and HL@Exo. Scale bar = 5 μm. (d) Zeta potential of Exo, HL, and HL@Exo. (e) Particle size distribution of Exo, HL, and HL@Exo. (f) Western blot analysis of exosome marker proteins (CD9, CD63 , CD81 and TSG101) in Exo and HL@Exo. (g) Cryo-TEM image of HL@Exo (phosphotungstic acid unstained), Scale bar = 2 μm.

increase in particle size over seven days, HL@Exo showed the smallest change, increasing from 239.12 nm to only 243.47 nm, with its PDI remaining essentially unchanged (0.178–0.176). This once again underscores the enhanced structural stability of HL@Exo compared to Exo (127.37–152.32 nm) and HL (164.33–195.68 nm) post-hybridization. This laid the foundation for enhancing the transdermal penetration and retention effect (EPR) of Exo in HL@Exo.

3.2. Kinetics of exosome penetration in skin tissues

The applicability of transdermal systems is typically demonstrated through permeability studies. The penetration efficiency, retention content, and duration of Exo in the skin are important criteria for evaluating the efficacy of HL@Exo. The Franz diffusion cell is widely used to determine the permeability of drugs through the skin. Therefore, a detailed analysis of the distribution of HL@Exo in skin tissues was conducted. Initially, a Franz diffusion cell was used to simulate *in vitro* penetration to determine the penetration efficiency of Exo and HL@Exo in the skin, as shown in Fig. 2b. The fluorescence intensity of Exo and HL@Exo was measured at 1 h, 3 h, 5 h, and 7 h. Compared to Exo, HL@Exo exhibited good penetration at 1 h, and the cumulative penetration of HL@Exo into the skin was significantly higher than that of Exo within 7 h. Skin sections were embedded and prepared as frozen slices for observation under a fluorescence microscope, revealing stronger fluorescence intensity in the HL@Exo group compared to the Exo group after 7 h, indicating higher penetration rates and retention contents in the HL@Exo group. Subsequently, *in vivo* imaging was employed to observe the penetration depth and distribution of Exo and HL@Exo in the skin of live mice. PKH-26 labeled Exo and HL@Exo were evenly applied to the surfaces of the mice's left and right legs, and muscle tissues from the administration sites were collected after 2 h. As shown in Figs. 2c and S2a, the fluorescence intensity in the thigh muscle tissue of mice treated with HL@Exo on the right side was significantly higher than that of mice treated with Exo on the left side. Additionally, longitudinal sections of the thigh skin tissue were observed to confirm the distribution of fluorescence in the skin tissue, consistent with the results from the Franz diffusion cell, indicating that HL hybridization significantly enhanced the penetration depth and retention content of Exo in the skin. Although mouse skin can be freshly excised before transdermal permeability studies, preserving enzymatic activity and exhibiting minimal variability, it is necessary to fully evaluate the transdermal efficacy of HL@Exo. Furthermore, an *in vitro* cell penetration model was utilized using HaCat cells to simulate the skin stratum corneum. HaCat cells were seeded in both the upper and lower chambers of Transwell, and multi-layered HaCat cells in the upper chamber were exposed to PKH26-labeled Exo and HL@Exo. The results are shown in Figs. 2d and S2b, pure Exo showed minimal penetration through the multi-layered HaCat cells, demonstrating poor penetration, while most HL@Exo penetrated the multi-layered HaCat cells. Therefore, this study, through the utilization of Franz diffusion cells, *in vivo* imaging, and *in vitro* cell penetration experiments, multidimensionally validated that HL hybridization significantly enhances the transdermal efficiency of Exo, potentially improving their utilization and laying the groundwork for future transdermal applications.

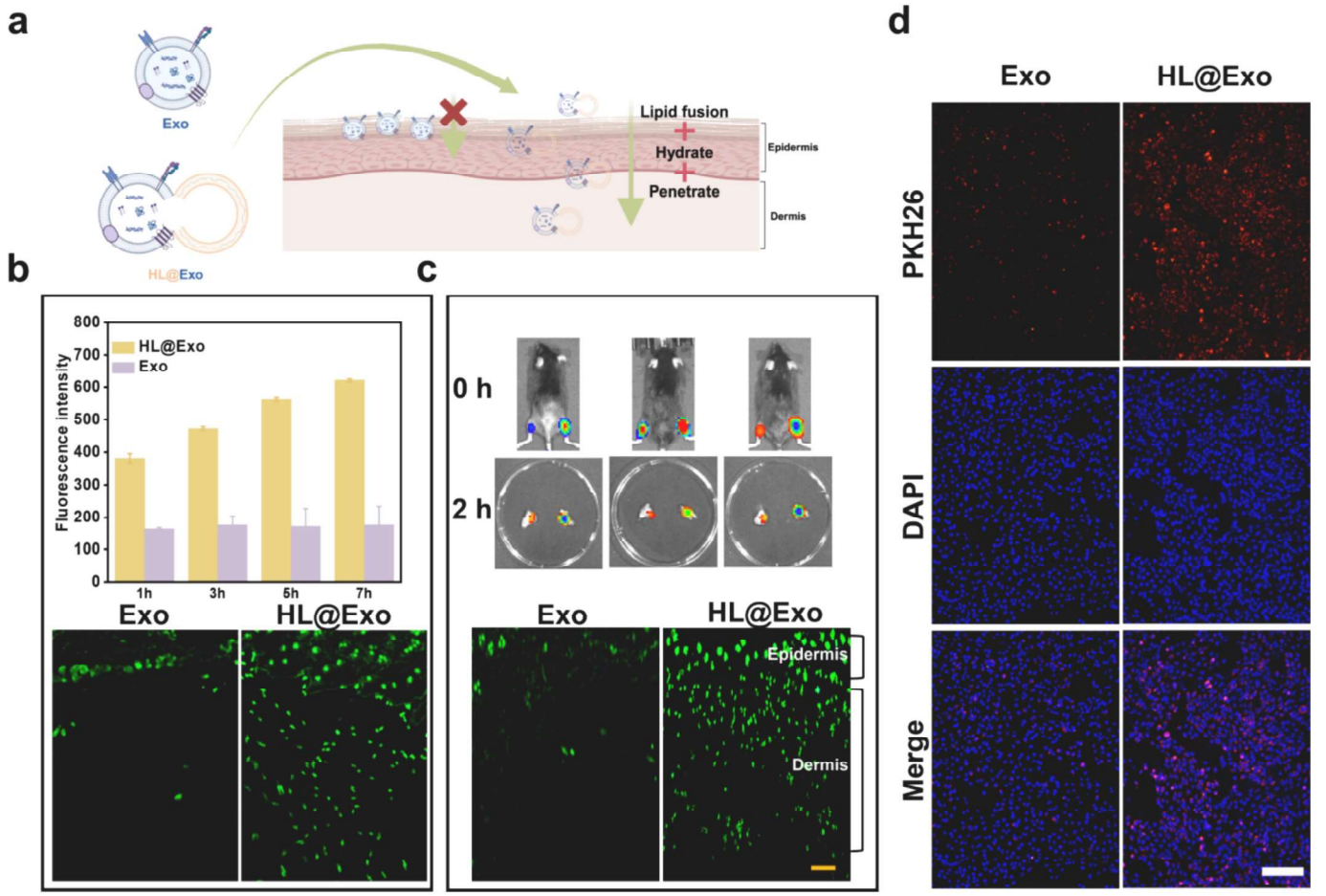

Fig. 2. Kinetics of exosome penetration in skin tissues. (a) Mechanism of HL enhancement of Exo penetration. (b) Quantitative fluorescence intensity and penetration distribution of Exo and HL@Exo at 1 h, 3 h, 5 h, and 7 h. (c) *In vivo* imaging of PKH-26-labeled Exo and HL@Exo in mouse skin. Scale bar = 100 μm. (d) Confocal microscopy of Exo and HL@Exo trans-multilayer cell penetration. Scale bar = 50 μm.

3.3. HL@Exo effectively enhances cell viability and inhibits apoptosis

To preliminarily validate the reparative function of HL@Exo on photodamaged skin, the proliferation of HaCat cells treated with HL@Exo for 24 h post-photodamage was assessed using the CCK-8 assay, as shown in Fig. 3b. Compared to the photodamaged control group (75.35 % ± 1.01), both Exo and HL@Exo exhibited certain cell proliferation effects, with percentages of (87.60 ± 1.32) % and (94.86 ± 1.60) %, respectively. Furthermore, compared to Exo and HL alone, HL@Exo demonstrated superior proliferation-promoting effects, providing a theoretical basis at the cellular level for the treatment of damaged skin [37]. Scratch assays depicted in Fig. 3(c, d) showed that compared to the photodamaged control group (52.42 % ± 2.42), both Exo and HL@Exo groups exhibited certain cell migration-promoting effects at 12 h and 24 h. Moreover, the reduction in scratch area after treatment with HL@Exo (77.9 % ± 2.34) at 24 h was significantly higher than that of the Exo group (61.98 % ± 0.798) and the HL group (54.83 % ± 2.92), further demonstrating the advantages of HL@Exo in enhancing skin cell vitality. To verify the efficacy of HL@Exo in inhibiting cell apoptosis, apoptosis was detected using live-dead staining after treatment with Exo, HL, and HL@Exo for UV-induced HaCaT apoptosis. Under irradiation, cell death significantly increased, while intervention with Exo, HL, and HL@Exo reduced HaCaT cell death (Fig. 3e). Under UV stimulation, excessive production of apoptotic factors in HaCaT cells can trigger oxidative stress, leading to apoptosis and tissue damage [38]. Damaged keratinocytes disrupt skin homeostasis, causing skin inflammation and worsening tissue injury. Therefore, inhibiting keratinocyte apoptosis is considered an effective strategy for preventing photodamage. RT-qPCR analysis revealed that UV exposure upregulated the expression of Caspase-3 and Bax. Compared to the control group, HL@Exo treatment significantly reduced the expression of these apoptosis-related factors. Furthermore, HL@Exo was more effective than Exo or HL alone in inhibiting UVB-induced HaCaT cell apoptosis (Fig. 3e). Studies suggest that exosomes derived from human umbilical mesenchymal stem cells can prevent acute kidney injury and other conditions by reducing apoptosis. This suggests that HL@Exo may improve UV-induced acute photodamage by inhibiting apoptosis and promoting cell proliferation. The pro-apoptotic Bcl-2 family member Bax plays a key role in the intrinsic mitochondrial apoptosis pathway by increasing mitochondrial membrane permeability, releasing apoptotic factors, and activating Caspase-3, the executor of apoptosis. The extrinsic apoptosis pathway, triggered by inflammatory cytokines such as IL-6, involves receptor interactions (TNFR, TLR4) that activate cell death pathways [39]. Although the exact mechanism by which HL@Exo repairs UV-induced apoptosis remains unclear, our study concludes that HL@Exo effectively suppresses the expression of multiple apoptosis factors involved in the intrinsic apoptosis cascade, thereby reversing apoptosis and improving UV-induced photodamage. This provides potential insights into the role of HL@Exo in improving UV-induced skin photodamage [40].

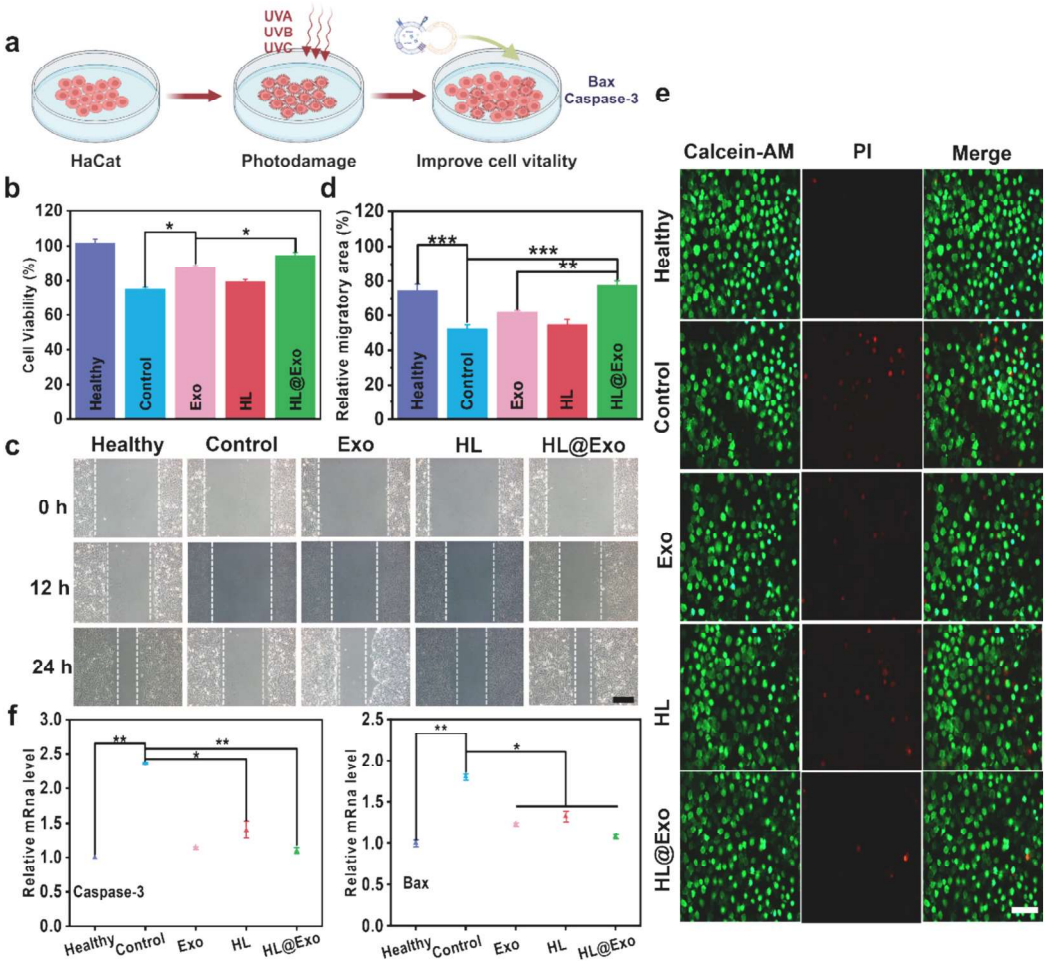

Fig. 3. HL@Exo's effect on photodamaged HaCat cells. (a) Mechanism of HL@Exo enhancing cell viability and inhibiting apoptosis. (b) Proliferation rates of photodamaged cells treated with Exo, HL, and HL@Exo. (c) Cell migration images. Scale bar = 100 μm. (d) Quantitative analysis of relative migration areas. (e) Live-dead cell staining images after Exo, HL, and HL@Exo treatment. Scale bar = 50 μm. (f) mRNA levels of Caspase-3, Bax in cells. $^{*}P < 0.05$; $^{**}P < 0.01$.

3.4. Effects of HL@Exo on oxidative damage in photodamaged cells

HaCat cells undergo oxidative stress under UV radiation, leading to changes in oxidative factors. The dynamic changes in SOD, CAT, and MDA play an important role in maintaining cellular homeostasis and function, regulating oxidative stress, and preventing or inhibiting skin inflammation, whose changes reflect the body's antioxidant potential [41]. As shown in Fig. 4b, compared to the healthy group, the activities of SOD and CAT significantly decreased in the control group, with the HL@Exo group showing levels closest to the healthy group. Additionally, we found that HL@Exo significantly reduced the intracellular MDA content compared to the control group. This indicates that HL@Exo effectively alleviates UV-induced oxidative stress in HaCaT cells, enhancing the levels of major antioxidant enzymes to approach normal levels. In addition, ultraviolet (UV) radiation not only induces oxidative stress but also triggers severe genotoxicity and a series of irreversible cellular damages. UV activation leads to excessive ROS generation within cells, which damages chromatin and induces DNA double-strand breaks. This damage severely affects cell viability and simultaneously triggers phosphorylation of the histone variant H2AX, rapidly generating γH2AX. The formation of γH2AX is an early marker of DNA damage response and reflects the extent of DNA damage in cells [42]. As shown in Fig. S3, compared to the healthy group, the control group cells subjected to only UV irradiation exhibited a significant and statistically significant increase in γH2AX expression. HaCaT cells treated with Exo and HL@Exo showed relatively weaker fluorescence intensity of γH2AX compared to the control group. Meanwhile, the γH2AX fluorescence intensity in photodamaged HaCaT cells treated with HL@Exos approached that of the healthy group, indicating that HL@Exo has a superior ability to alleviate UV radiation-induced DNA damage and genetic toxicity compared to HL [43]. IGF-1 is an important regulator of cell growth and proliferation, and increasing evidence suggests its significant role in wound healing [44,45]. As shown in Fig. 4c, compared to the control group, although the HL, Exo, and HL@Exo treatment groups showed higher levels of IGF-1 expression than the control group, only the HL@Exo treatment group exhibited IGF-1 expression closest to the healthy group. This indicates that HL@Exo effectively mitigates the loss of cell vitality induced by UV radiation, demonstrating superior protective effects. Based on the above research, HL@Exo demonstrates significant antioxidant activity, alleviates genotoxicity, and promotes cell repair. These findings provide potential new insights into the application of HL@Exo in the protective mechanisms against UV-induced cellular damage.

3.5. Effects of HL@Exo on angiogenesis

Numerous studies have demonstrated that angiogenesis is beneficial for forming stable matrix scaffolds that provide essential support for new tissue, thereby promoting wound healing [29]. In this study, we evaluated the effects of HL, Exo, and HL@Exo on HUVECs. First, the CCK-8 assay was used to detect cell proliferation after 24 h of treatment with Exo, HL, and HL@Exo. As shown in Fig. 5b, compared to the healthy group, the Exo, HL, and HL@Exo groups all exhibited certain cell proliferation effects, with HL@Exo showing significant effects, achieving a cell proliferation rate of 141.99 ± 1.95 %. Additionally, the scratch migration assay, as shown in Fig. 5(c, e), indicated that compared to the healthy group, the Exo, HL, and HL@Exo groups all promoted cell migration at 12 h and 24 h, with HL@Exo significantly reducing the scratch area (78.33 % ±3.05) after 24 h, outperforming both the Exo and HL groups. This indicates that HL@Exo has superior proliferation and migration capabilities. Furthermore, these conclusions were validated in the tube formation assay. As shown in Fig. 5(d, f, g), the HL@Exo group promoted the formation of more nodes and complete tubular structures compared to the other treatment groups. These results demonstrate that HL@Exo, with its sustained release properties, effectively promotes angiogenesis, highlighting its potential role in wound healing.

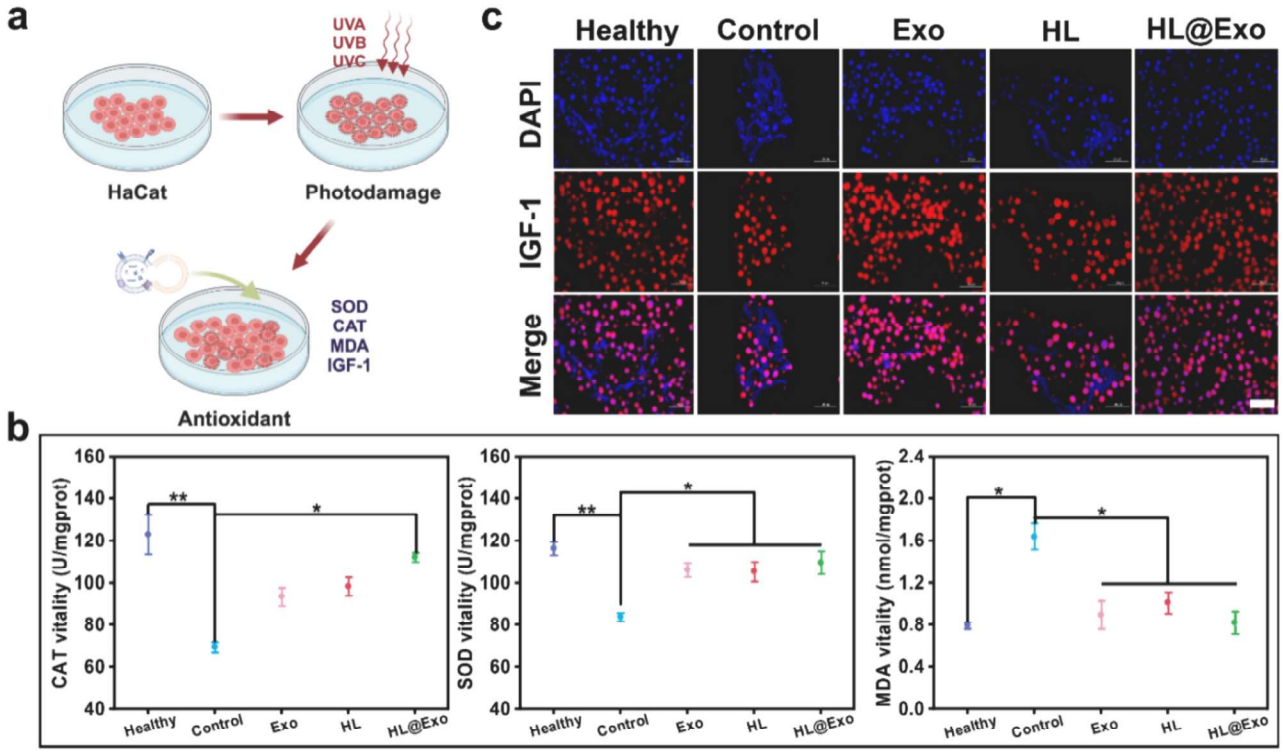

Fig. 4. Effects of HL@Exo on oxidative damage in photodamaged cells. (a) Mechanism of HL@Exo improving oxidative stress in photodamaged cells. (b) Levels of CAT, SOD, and MDA in each group. (c) Fluorescent expression of IGF-1 in various groups of cells, scale bar = 50 μm. *$P < 0.05$; **$P < 0.01$.

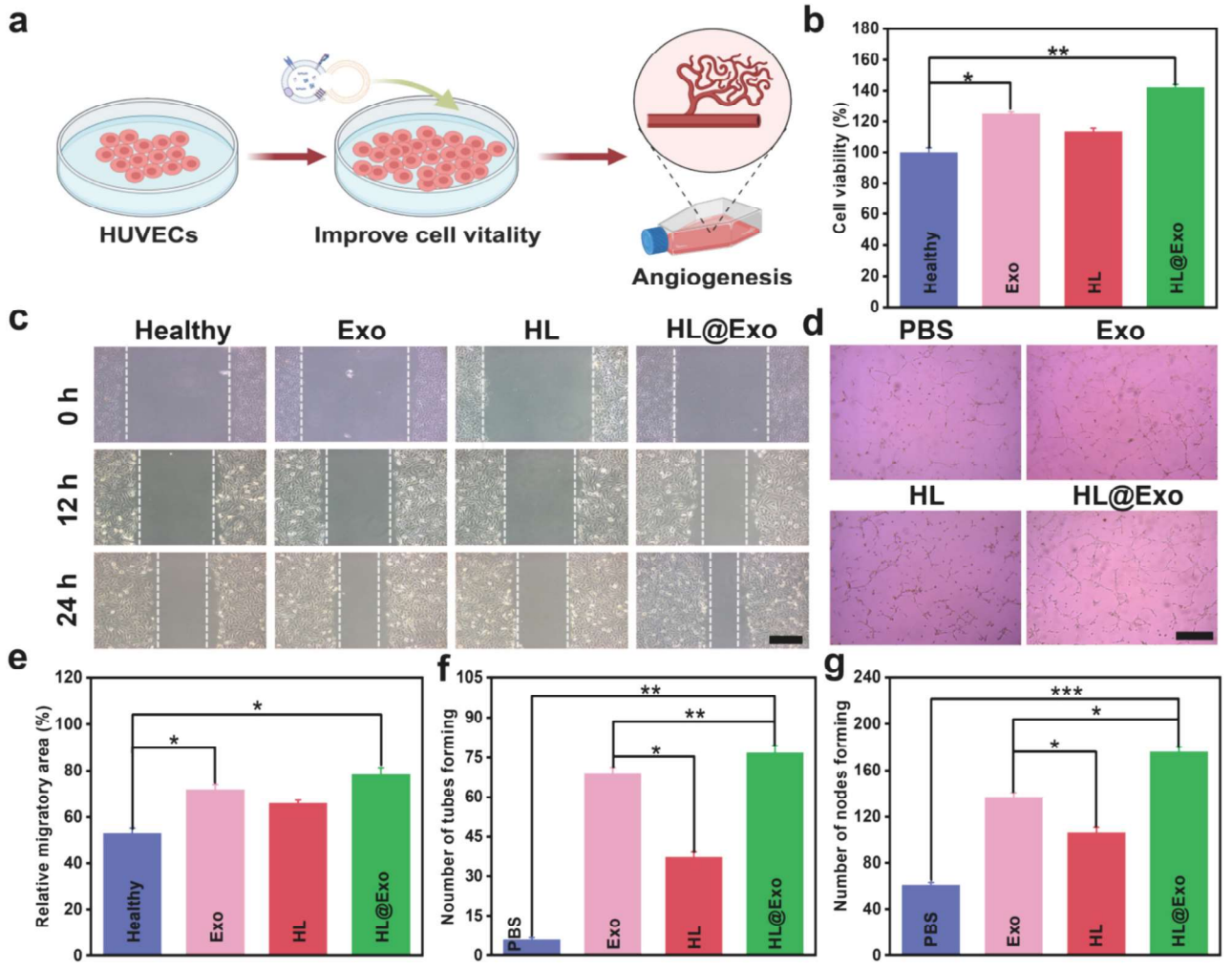

Fig. 5. Effects of HL@Exo on HUVECs. (a) Schematic of HL@Exo promoting angiogenesis. (b) Proliferation rates of HUVECs treated with Exo, HL, and HL@Exo. (c) Cell migration images. Scale bar = 100 μm. (d) Optical images of tube formation in HUVECs under different treatments. Scale bar = 200 μm. (e) Quantitative analysis of relative migration areas in each group. (f) Quantitative analysis of the total number of meshes formed. (g) Quantitative analysis of the total number of nodes formed. $^{*}P < 0.05$; $^{**}P < 0.01$; $^{***}P < 0.001$.

3.6. Overall evaluation of HL@Exo in treating acute skin photodamage

In the aforementioned cellular experiments, we successfully validated the advantages of HL@Exo in combating cellular oxidation and enhancing cell vitality. To investigate the potential of HL@Exo in repairing damaged skin and modulating skin inflammation, we chose to construct a laser point array-induced acute skin injury model and conducted a 7-day treatment period. During this period, observations and records were made on the physiological status of mice, skin repair conditions, and distribution of exosomes. Following the experiment's conclusion, histopathological sections were collected to evaluate the reparative effect of HL@Exo on acutely laser-injured skin. As depicted in Figs. 6b and S4, on the first day of modeling, the skin of mice in the healthy group showed no redness or scarring, while mice in other laser-injured groups exhibited significant exudation and scabbing. By the third day post-modeling, the model group exhibited the most severe redness and congestion, whereas compared to the Exo and HL groups, the HL@Exo group showed milder redness and rupture. Under skin microscopy, the improvement in the HL@Exo group was most notable. From the fifth to the seventh day post-modeling, mice in the HL and HL@Exo groups exhibited nearly complete wound healing, while the model group and Exo group still had partial wounds. At the same time, we used the clinically proven drug Snow Lotus Cream Ointment (SHYNDEC) as a positive control group and compared it with the HL@Exo group. SHYNDEC indeed showed some reparative effects, but its therapeutic effect was significantly inferior compared to the HL@Exo group, as shown in Fig. S4. Additionally, validation of skin injury quantification was obtained through Image J analysis, as depicted in Fig. S5(b, c). Furthermore, Following the construction of the mouse acute laser point array injury model, locally applied treatment with PKH26-labeled Exo and HL@Exo was administered to the damaged skin. After 12 h of treatment, skin from the back was collected, as shown in Fig. S6(a, b). It was evident that under damaged skin conditions, HL@Exo achieved prolonged residency in the skin. Quantitative analysis revealed that the fluorescence ratio of HL@Exo in the skin was significantly higher than that of Exo, ensuring the sustained efficacy of exosomes and further facilitating the repair of acutely photo-damaged skin (Fig. S6c). This ensures the prolonged efficacy of the active substances within HL@Exo, further confirming its potential as an excellent wound healing material.

3.7. Histological analysis of HL@Exo promoting photodamage skin repair

To determine the regulatory effects of HL@Exo on skin inflammation and the deep tissue repair of mouse skin, we conducted detailed histological analysis of post-treatment skin samples. [46]. As shown in Figs. 7 and S7a, epidermal thickness was quantitatively assessed as a measure of skin photodamage severity [47]. Compared to the healthy group,

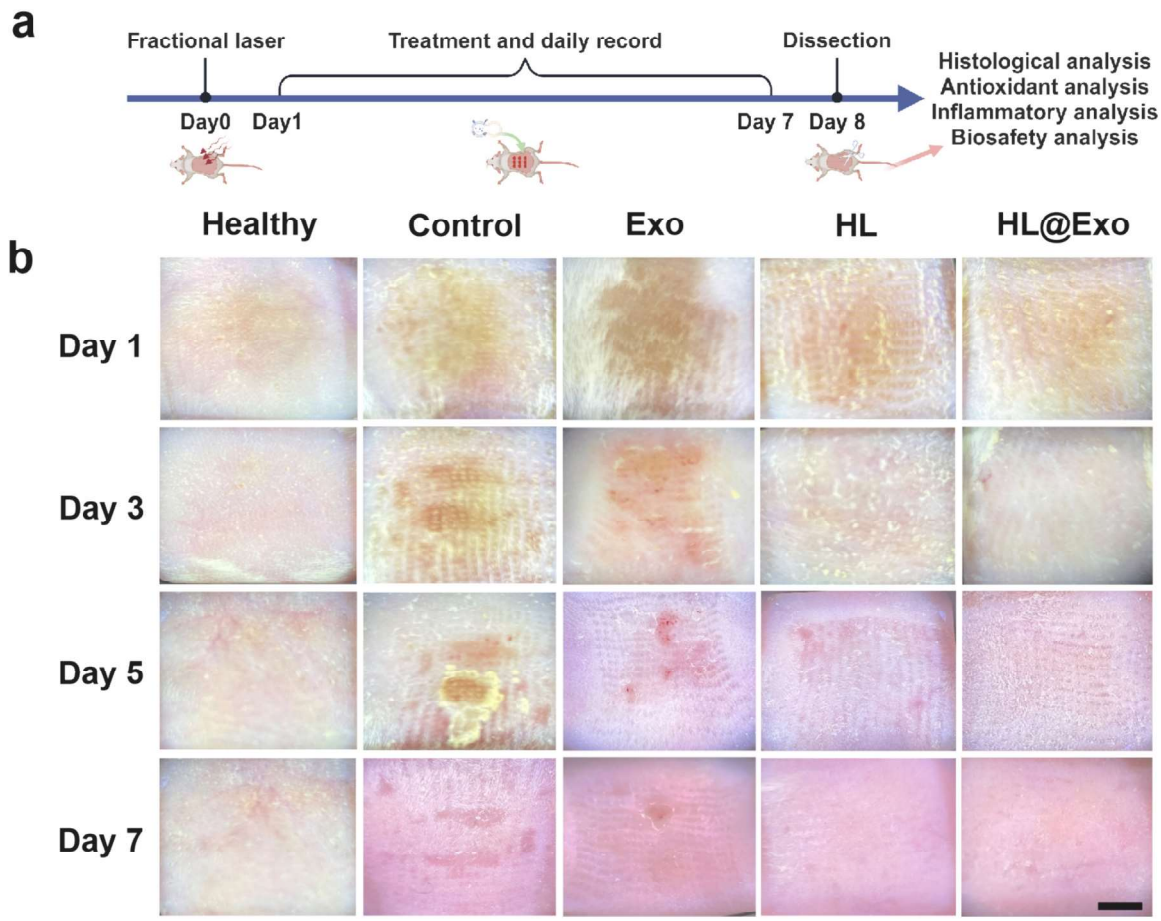

Fig. 6. Overall evaluation of acute photodamage skin treatment. (a) Establishment and subsequent treatment of a mouse acute photodamage model. (b) Dermatoscope images of mouse skin treated with PBS, Exo, HL, and HL@Exo for 7 days post-laser injury. Scale bar = 500 mm.

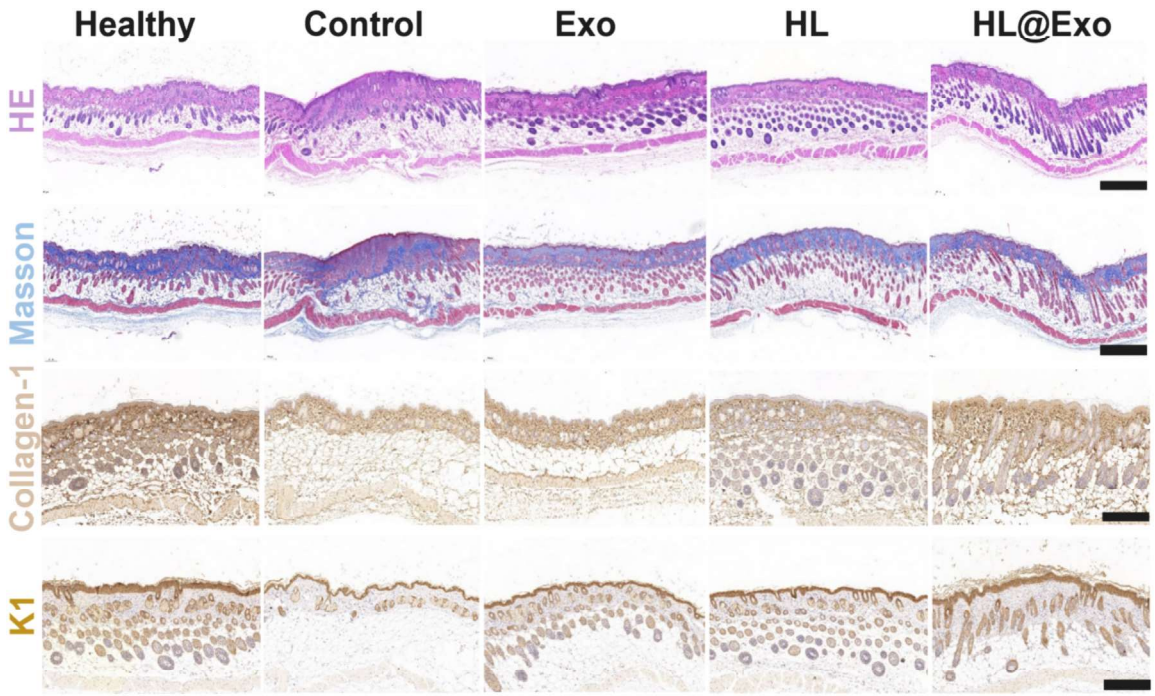

Fig. 7. Histological analysis of HL@Exo promoting skin repair. From top to bottom: H&E staining, Masson staining, Collagen-1 immunohistochemical staining, and K1 immunohistochemical staining. Scale bars = 200 μm, 200 μm, 100 μm, 100 μm, respectively.

mice in the model group exhibited significantly increased epidermal thickness, exceeding that of the healthy group by >6 times. This change is a direct manifestation of the inflammatory response in keratinocytes induced by ultraviolet (UV) radiation. In the model group, the connection between the epidermis and dermis was severely disrupted, with a significant infiltration of inflammatory cells in the dermis. However, in the HL@Exo group, the epidermal thickness was significantly reduced, approaching the level seen in the healthy group. This result indicates that HL@Exo can effectively suppress the inflammatory response and restore the structural integrity of the skin barrier. Additionally, the connection between the epidermis and dermis in the HL@Exo group was tighter, and the dermal structure was more uniform, further validating its advantages in tissue repair. Masson staining was used to evaluate the arrangement and density of collagen fibers. The results showed that in the model group, the collagen fibers were disorganized and the density was significantly decreased, which is a typical feature of UV-induced skin damage. In contrast, the HL@Exo treatment group showed well-organized collagen fibers with density restored, similar to the healthy group. This indicates that HL@Exo significantly improves the structural integrity of the dermis by modulating collagen fiber composition. Combined with the analysis of Collagen-1 expression, the HL@Exo group showed a significant upregulation of collagen expression, further confirming its ability to promote ECM recovery. Furthermore, we investigated the expression changes of keratin K1 in UV-damaged skin. Keratin K1 is a major component of epidermal structural proteins, and its reduction often reflects skin barrier damage and impaired healing capacity [48]. In the model group, both keratin K1 and collagen expression were significantly reduced, whereas in the HL@Exo group, the levels of both were significantly restored, close to those seen in the healthy group. This result was further validated by quantitative analysis using Image J 5.0 (Additional Fig. 7). This indicates that the active substances in HL@Exo play a key role in the reconstruction of the epidermal barrier and structural repair. Ki67 and PCNA are proliferation-related markers, with PCNA playing a critical role in cell proliferation and DNA repair. VEGF is a specific factor and key mediator of angiogenesis in cells, with high expression reflecting active cell proliferation and pro-angiogenic capacity. As shown in Figs. 8(a, b) and S8, compared to the model group, the expression of Ki67, VEGF, and PCNA was significantly increased in the skin tissue surrounding the HL@Exo-treated mice, indicating enhanced cell proliferation and blood vessel formation [49,50]. This suggests that HL@Exo effectively promotes cell proliferation and angiogenesis, accelerating skin regeneration and repair. Moreover, through TUNEL fluorescence staining to assess cell apoptosis (Fig. 8c), the model group exhibited the highest number of apoptotic cells, whereas the HL@Exo group showed a significant reduction in apoptotic cells, approaching the level seen in the healthy group. This suggests that HL@Exo provides a more stable cellular environment in the skin injury area by inhibiting apoptosis, thereby further promoting wound repair. In conclusion, this study successfully constructed an acute UV-induced skin damage animal model and systematically evaluated the multi-dimensional mechanisms of HL@Exo in skin repair. The results indicate that HL@Exo can promote skin tissue regeneration and structural repair by inhibiting the inflammatory response, collagen fiber organization, and skin microenvironment, repairing the epidermal barrier, and regulating cell proliferation and apoptosis. These findings provide strong support for its application as an effective skin treatment strategy.

3.8. HL@Exo effectively regulates lipid peroxidation and inflammatory responses

UV-induced photodamage not only leads to a significant increase in oxidative stress levels in the skin but also induces the excessive secretion of pro-inflammatory cytokines, triggering a skin inflammatory response. In this study, by measuring the levels of TNF-α, IL-6, and IL-1β in mouse skin tissue [51], we found that the levels of inflammatory cytokines were significantly elevated in the model group, indicating that UV radiation induced acute inflammatory responses and immune imbalance. In contrast, the levels of inflammatory cytokines in the HL@Exo group were close to those in the healthy group, suggesting that HL@Exo can

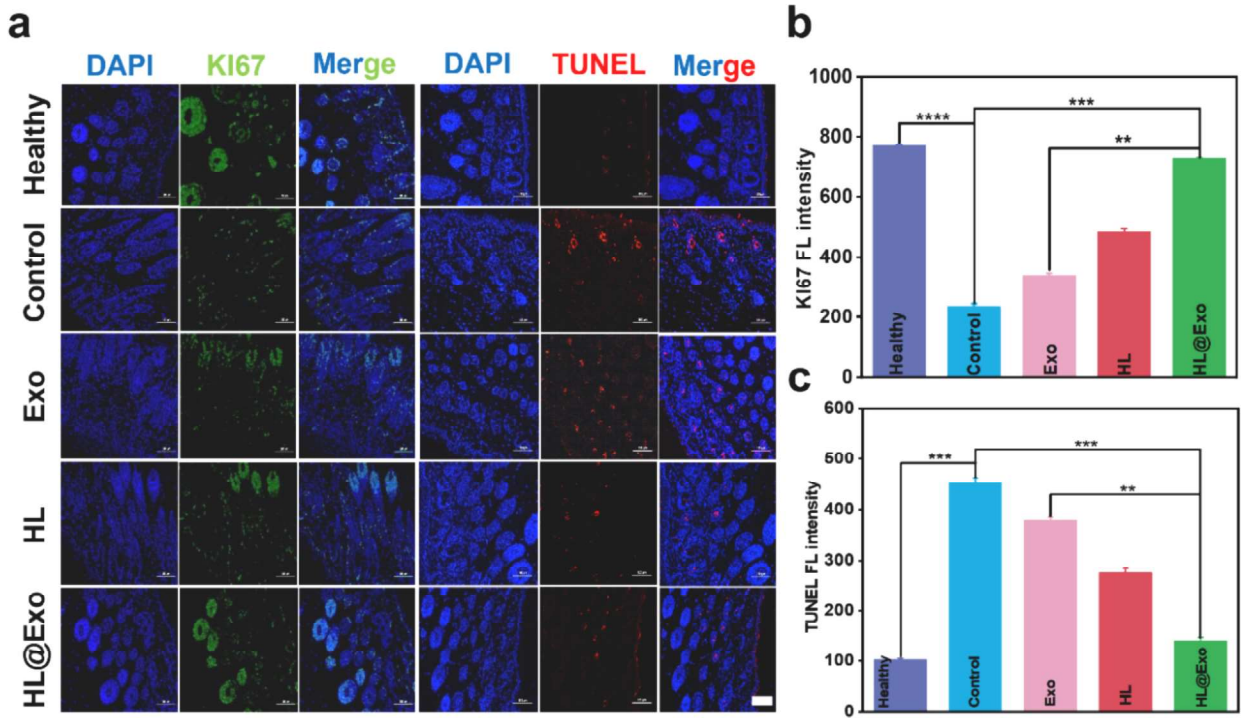

Fig. 8. Evaluation of HL@Exo in inflammation regulation and repair in mice. (a) Fluorescence expression of Ki67 and TUNEL in mouse skin in each group. Scale bar = 100 μm. (b) Quantitative analysis of Ki67 fluorescence intensity. (c) Quantitative analysis of TUNEL fluorescence intensity. *$P < 0.05$; **$P < 0.01$; ***$P < 0.001$; ****$P < 0.0001$.

significantly inhibit the release of pro-inflammatory cytokines and restore the balance of the inflammatory microenvironment. This anti-inflammatory effect is attributed to the synergistic action of the active molecules in HL@Exo, which effectively suppress inflammation. Furthermore, oxidative stress is one of the key mechanisms underlying UV-induced photodamage. The elevated levels of lipid peroxidation product MDA and the decreased activity of antioxidant enzyme SOD are typical indicators of oxidative stress [52]. In the previous cell experiments, HL@Exo demonstrated significant antioxidant capacity, and in this study, its antioxidant effect *in vivo* was further validated through enzyme-linked immunosorbent assays (ELISA) of skin tissue. As shown in Figs. 9(d, e), compared to the model group, the MDA content in the HL@Exo-treated group was significantly reduced, while the SOD level was significantly increased, approaching that of the healthy group. This suggests that HL@Exo can effectively alleviate oxidative stress damage induced by acute photodamage, and its mechanism may involve inhibiting lipid peroxidation and enhancing the activity of the cellular antioxidant enzyme system. In summary, the anti-inflammatory and antioxidant effects of HL@Exo are synergistic in nature. On one hand, by increasing the SOD levels and reducing the generation of MDA, HL@Exo mitigates the oxidative stress-induced damage to skin cell membranes, DNA, and proteins, thus inhibiting the excessive production of inflammatory cytokines [53,54]. On the other hand, by directly down-regulating the levels of inflammatory cytokines, HL@Exo modulates the immune balance in the damaged area, restoring the normal immune microenvironment of the skin tissue. This potential dual mechanism provides an important therapeutic strategy for alleviating skin damage caused by photodamage.

3.9. Analysis of material biocompatibility

Biosafety is a crucial prerequisite for the biomedical application and subsequent clinical translation of biomaterials. To assess the biosafety of HL@Exo, the skin condition of mice after local application of the material was observed initially. As shown in Fig. 10a, after three days of treatment with Exo, HL, and HL@Exo, no dryness, desquamation, erythema, or edema were observed on the skin of mice. Furthermore, following the conclusion of the acute photodamage experiment, the hearts, livers, spleens, lungs, and kidneys of mice from all groups were subjected to H&E staining. As depicted in Fig. 10b, no damage or toxicity was observed in the tissues of mice from all groups. Finally, biochemical markers (AST, ALT, LDH, UA, CR, GLU) were measured in the blood of mice from different groups to assess organ damage. The results in Fig. 10c demonstrate that all parameters in the treatment groups were within the normal range compared to the healthy group. Therefore, these results indicate that HL@Exo exhibits excellent biosafety and holds potential value for clinical application.

4. Conclusion

In this study, a novel hyaluronic acid-liposome-exosome transdermal system (HL@Exo) was successfully constructed using ultrasonic incubation combined with membrane extrusion technology, significantly enhancing the therapeutic potential of exosomes (Exo) in acute skin injury. The successful hybridization of HL@Exo was verified through fluorescence labeling and immunoblotting, and further confirmed by *in vivo* imaging and Transwell assays, demonstrating its efficient penetration and prolonged retention of Exo in the skin. Additionally, *in vitro* experiments on UV-induced human keratinocytes (HaCaT) showed that HL@Exo promotes cell viability and inhibits the activation of pro-apoptotic factors. In human umbilical vein endothelial cells (HUVECs), HL@Exo was shown to promote angiogenesis and regulate the damaged microenvironment. In a laser-induced acute skin injury model, HL@Exo significantly improved oxidative stress, inhibited apoptosis, and modulated the inflammatory response, demonstrating its great potential in promoting skin barrier repair and wound healing. Biosafety assessments confirmed that HL@Exo has good biocompatibility. Compared with other types of nanocarriers, such as polymer nanoparticles, dendrimers, or micelles, HL@Exo enhances its permeability in the stratum corneum through hyaluronic acid liposomes and improves the sustained release of exosomes by utilizing its sustained-release properties. HL@Exo's ability to synergistically regulate

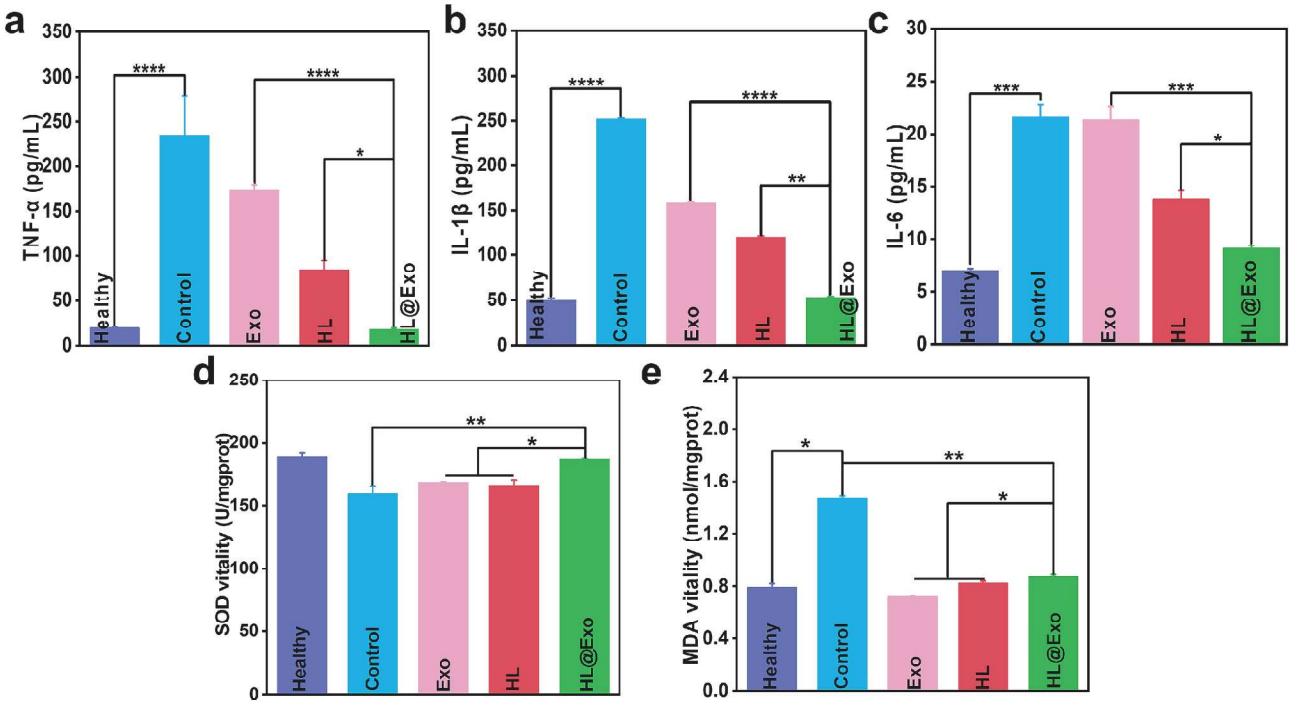

Fig. 9. Evaluation of HL@Exo inhibiting lipid peroxidation and inflammatory response. (a) TNF-α content in mouse skin in each group. (b) IL-1β content in mouse skin in each group. (c) IL-6 content in mouse skin in each group. (d) SOD activity in mouse skin in each group. (e) MDA content in mouse skin in each group. *$P < 0.05$; **$P < 0.01$; ***$P < 0.001$; ****$P < 0.0001$.

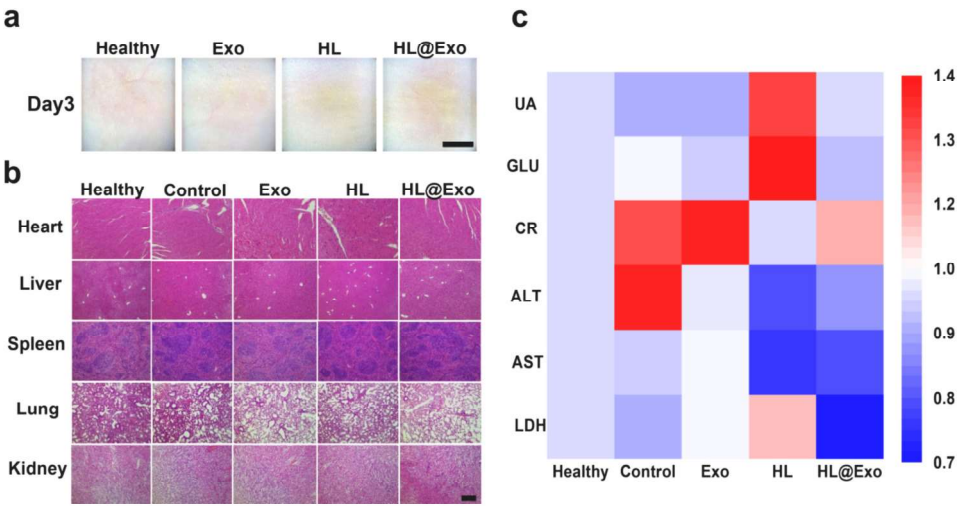

Fig. 10. Evaluation of material biocompatibility. (a) Skin condition under a dermatoscope after three consecutive days of treatment. Scale bar = 500 mm. (b) Histopathological examination of major organs (heart, liver, spleen, lung, and kidney) from five groups of mice receiving different treatments. Scale bar = 100 μm. (c) Analysis of liver function (ALT, AST, LDH), kidney function (UA, CR), blood glucose (GLU), and blood biochemical indicators in different groups of mice.

oxidative stress and inflammation while promoting tissue regeneration highlights its multifunctionality. Although safety has been evaluated, further research is needed to assess its long-term safety and scalability for large-scale production. In conclusion, HL@Exo provides a novel strategy for the non-invasive application of Exo in the treatment of acute skin damage, offering significant clinical translation potential and broad application prospects.

CRediT authorship contribution statement

Yuhui Yang: Writing – review & editing, Writing – original draft, Validation, Methodology, Formal analysis, Data curation. **Yong He:** Supervision, Resources, Formal analysis, Data curation. **Hui Xing:** Methodology, Data curation. **Ziyi Zhao:** Methodology, Investigation, Data curation. **Jianjin Wang:** Software, Resources, Funding acquisition. **Shanying Li:** Resources, Investigation, Funding acquisition. **Xiaosong Xu:** Resources, Funding acquisition. **Dong Ma:** Resources, Methodology, Investigation, Funding acquisition. **Yunfeng Hu:** Supervision, Resources, Funding acquisition, Data curation.

Declaration of competing interest

The authors declare that they have no known competing financial interests.

Acknowledgments

This work was financially supported by the National Natural Science Foundation of China (32171369), the Preliminary Study on Exosome-Liposome Hybrid Nanovesicles for Transdermal Applications (ZX20230712), Guangzhou Science and Technology Bureau City-School (Institute)-Enterprise Joint Project (2023A03J0618 and basic operating expenses of the Central Colleges and Universities of Jinan University (11623410). The authors would also like to thank BioRender (www.biorender.com) for assistance with Fig. preparation.

Appendix A. Supplementary data

Supplementary data to this article can be found online at https://doi.org/10.1016/j.ijbiomac.2025.141606.

References

[1] R.G. Dare, M.M. Oliveira, M.C. Truiti, C.V. Nakamura, V.F. Ximenes, S. O. Lautenschlager, Abilities of protocatechuic acid and its alkyl esters, ethyl and heptyl protocatechuates, to counteract UVB-induced oxidative injuries and photoaging in fibroblasts L929 cell line, J. Photochem. Photobiol. B Biol. 203 (2020) 111771.
[2] C. Marionnet, C. Tricaud, F. Bernerd, Exposure to non-extreme solar UV daylight: spectral characterization, effects on skin and photoprotection, Int. J. Mol. Sci. 16 (1) (2014) 68–90.
[3] M. Oyama, K. Murata, M. Ogata, N. Fujita, R. Takahashi, Saireito improves lymphatic function and prevents UVB-induced acute inflammation and photodamage in HR-1 hairless mice, Evid. Based Complement. Alternat. Med. 2021 (2021).
[4] C. Antille, C. Tran, O. Sorg, P. Carraux, L. Didierjean, J.-H. Saurat, Vitamin a exerts a photoprotective action in skin by absorbing ultraviolet B radiation, Journal of Investigative Dermatology 121 (5) (2003) 1163–1167.
[5] B. Zhang, X. Wu, X. Zhang, Y. Sun, Y. Yan, H. Shi, Y. Zhu, L. Wu, Z. Pan, W. Zhu, Human umbilical cord mesenchymal stem cell exosomes enhance angiogenesis through the Wnt4/β-catenin pathway, Stem Cells Transl. Med. 4 (5) (2015) 513–522.
[6] Z. Xunian, R. Kalluri, Biology and therapeutic potential of mesenchymal stem cell-derived exosomes, Cancer Sci. 111 (9) (2020) 3100–3110.
[7] Y. Hu, S.-S. Rao, Z.-X. Wang, J. Cao, Y.-J. Tan, J. Luo, H.-M. Li, W.-S. Zhang, C.-Y. Chen, H. Xie, Exosomes from human umbilical cord blood accelerate cutaneous wound healing through miR-21-3p-mediated promotion of angiogenesis and fibroblast function, Theranostics 8 (1) (2018) 169.
[8] X. Zhang, P. Ding, Y. Chen, Z. Lin, X. Zhao, H. Xie, Human umbilical cord mesenchymal stem cell-derived exosomes combined with gelatin methacryloyl hydrogel to promote fractional laser injury wound healing, Int. Wound J. 20 (10) (2023) 4040–4049.
[9] A.Z. Alkilani, J. Nasereddin, R. Hamed, S. Nimrawi, G. Hussein, H. Abo-Zour, R. F. Donnelly, Beneath the skin: a review of current trends and future prospects of transdermal drug delivery systems, Pharmaceutics 14 (6) (2022) 1152.
[10] H. Xing, X. Pan, Y. Hu, Y. Yang, Z. Zhao, H. Peng, J. Wang, S. Li, Y. Hu, G. Li, High molecular weight hyaluronic acid-liposome delivery system for efficient transdermal treatment of acute and chronic skin photodamage, Acta Biomater. 182 (2024) 171–187.
[11] J. Malakar, S.O. Sen, A.K. Nayak, K.K. Sen, Formulation, optimization and evaluation of transferosomal gel for transdermal insulin delivery, Saudi pharmaceutical journal 20 (4) (2012) 355–363.
[12] M. Kurakula, O.A. Ahmed, U.A. Fahmy, T.A. Ahmed, Solid lipid nanoparticles for transdermal delivery of avanafil: optimization, formulation, in-vitro and ex-vivo studies, J. Liposome Res. 26 (4) (2016) 288–296.
[13] M.L. Manca, I. Castangia, M. Zaru, A. Nácher, D. Valenti, X. Fernàndez-Busquets, A. Fadda, M. Manconi, Development of curcumin loaded sodium hyaluronate immobilized vesicles (hyalurosomes) and their potential on skin inflammation and wound restoring, Biomaterials 71 (2015) 100–109.
[14] Y. Wang, Z. Tang, X. Guo, Y. Zhao, S. Ren, Z. Zhang, H. Lv, Hyaluronic acid-cyclodextrin encapsulating paeonol for treatment of atopic dermatitis, Int. J. Pharm. 623 (2022) 121916.
[15] H. Xing, H. Peng, Y. Yang, K. Lv, S. Zhou, X. Pan, J. Wang, Y. Hu, G. Li, D. Ma, Nitric oxide synergizes minoxidil delivered by transdermal hyaluronic acid liposomes for multimodal androgenetic-alopecia therapy, Bioactive Materials 32 (2024) 190–205.

[16] M.E. Cano, D. Lesur, V. Bincoletto, E. Gazzano, B. Stella, C. Riganti, S. Arpicco, J. Kovensky, Synthesis of defined oligohyaluronates-decorated liposomes and interaction with lung cancer cells, Carbohydr. Polym. 248 (2020) 116798.
[17] L. Sun, M. Fan, D. Huang, B. Li, R. Xu, F. Gao, Y. Chen, Clodronate-loaded liposomal and fibroblast-derived exosomal hybrid system for enhanced drug delivery to pulmonary fibrosis, Biomaterials 271 (2021) 120761.
[18] Y.-Y. Jhan, D. Prasca-Chamorro, G.P. Zuniga, D.M. Moore, S.A. Kumar, A. K. Gaharwar, C.J. Bishop, Engineered extracellular vesicles with synthetic lipids via membrane fusion to establish efficient gene delivery, Int. J. Pharm. 573 (2020) 118802.
[19] A. Singh, A. Raghav, P.A. Shiekh, A. Kumar, Transplantation of engineered exosomes derived from bone marrow mesenchymal stromal cells ameliorate diabetic peripheral neuropathy under electrical stimulation, Bioactive Materials 6 (8) (2021) 2231–2249.
[20] H. Hu, W. Zhang, Y. Zhou, K. Zhao, J. Kuang, X. Liu, G. Li, Y. Xi, Engineered mitochondrial ROS scavenger nanocomplex to enhance lung biodistribution and reduce inflammation for the treatment of ARDS, Adv. Compos. Hybrid Mater. 7 (6) (2024) 194.
[21] K. Zhao, L. Qi, Q. Li, Y. Wang, C. Qian, Z. Shi, Self-absorbing multilayer skin-like composite with Phyllostachys nigra polysaccharides promotes wound healing, Advanced Composites and Hybrid Materials 7 (6) (2024) 225.
[22] M. Kumar, A. Sharma, S. Mahmood, A. Thakur, M.A. Mirza, A. Bhatia, Franz diffusion cell and its implication in skin permeation studies, J. Dispers. Sci. Technol. (2023) 1–14.
[23] Y. Zeng, Y. Song, J. Li, W. Zhang, B. Shi, Visualization and quantification of penetration/mass transfer of acrylic resin Retanning agent in leather using florescent tracing technique, J. Am. Leather Chem. Assoc. 111 (11) (2016) 398–405.
[24] C. Ni, Z. Zhang, Y. Wang, Z. Zhang, X. Guo, H. Lv, Hyaluronic acid and HA-modified cationic liposomes for promoting skin penetration and retention, J. Control. Release 357 (2023) 432–443.
[25] Y. Ni, W. Zhao, W. Cheng, C. Deng, Z. Ying, L. Li, X. Wang, C. Sun, J. Tu, L. Jiang, Lipopeptide liposomes-loaded hydrogel for multistage transdermal chemotherapy of melanoma, J. Control. Release 351 (2022) 245–254.
[26] L. Cheng, J. Liu, Q. Wang, H. Hu, L. Zhou, The protective effect of a human umbilical cord mesenchymal stem cell supernatant on UVB-induced skin Photodamage, Cells 13 (2) (2024) 156.
[27] F. Bai, C. Fan, X. Lin, H.-Y. Wang, B. Wu, C.-L. Feng, R. Zhou, Y.-W. Wu, W. Tang, Hemin protects UVB-induced skin damage through inhibiting keratinocytes apoptosis and reducing neutrophil infiltration, J. Photochem. Photobiol. B Biol. 238 (2023) 112604.
[28] V.-L. Truong, Y.-J. Bae, J.-H. Bang, W.-S. Jeong, Combination of red ginseng and velvet antler extracts prevents skin damage by enhancing the antioxidant defense system and inhibiting MAPK/AP-1/NF-κB and caspase signaling pathways in UVB-irradiated HaCaT keratinocytes and SKH-1 hairless mice, J. Ginseng Res. 48 (3) (2024) 323–332.
[29] H. Peng, H. Li, X. Zhang, J. Tang, Y. Liang, L. Qiao, Y. Zhu, M. Hou, S. Wei, Z. Zhang, 3D-exosomes laden multifunctional hydrogel enhances diabetic wound healing via accelerated angiogenesis, Chem. Eng. J. 475 (2023) 146238.
[30] Y. Xie, J. He, S. Li, X. Chen, T. Zhang, Y. Zhao, Y. Lin, X. Cai, A transdermal drug delivery system based on nucleic acid nanomaterials for skin photodamage treatment, Adv. Funct. Mater. 33 (46) (2023) 2303580.
[32] N. Dragicevic, H. Maibach, Combined use of nanocarriers and physical methods for percutaneous penetration enhancement, Adv. Drug Deliv. Rev. 127 (2018) 58–84.
[33] U.K. Sur, Recent trends in materials: physics and chemistry, Studium press (India) Pvt. Limited2019.
[34] A. Liu, G. Yang, Y. Liu, T. Liu, Research progress in membrane fusion-based hybrid exosomes for drug delivery systems, Front. Bioeng. Biotechnol. 10 (2022) 939441.
[35] S. Rayamajhi, T.D.T. Nguyen, R. Marasini, S. Aryal, Macrophage-derived exosome-mimetic hybrid vesicles for tumor targeted drug delivery, Acta Biomater. 94 (2019) 482–494.
[36] K. Song, Y. Hao, X. Tan, H. Huang, L. Wang, W. Zheng, Microneedle-mediated delivery of Ziconotide-loaded liposomes fused with exosomes for analgesia, J. Control. Release 356 (2023) 448–462.
[37] Y. Kawano, V. Patrulea, E. Sublet, G. Borchard, T. Iyoda, R. Kageyama, A. Morita, S. Seino, H. Yoshida, O. Jordan, Wound healing promotion by hyaluronic acid: effect of molecular weight on gene expression and in vivo wound closure, Pharmaceuticals 14 (4) (2021) 301.
[38] F. Afaq, D.N. Syed, A. Malik, N. Hadi, S. Sarfaraz, M.-H. Kweon, N. Khan, M. A. Zaid, H. Mukhtar, Delphinidin, an anthocyanidin in pigmented fruits and vegetables, protects human HaCaT keratinocytes and mouse skin against UVB-mediated oxidative stress and apoptosis, J. Invest. Dermatol. 127 (1) (2007) 222–232.
[39] L. Li, S. Wang, W. Zhou, Balance cell apoptosis and pyroptosis of caspase-3-activating chemotherapy for better antitumor therapy, Cancers 15 (1) (2022) 26.
[40] N. Üremiş, M. Aslan, E. Taşlidere, E. Gürel, Dexpanthenol exhibits antiapoptotic and anti-inflammatory effects against nicotine-induced liver damage by modulating Bax/Bcl-xL, Caspase-3/9, and Akt/NF-κB pathways, J. Biochem. Mol. Toxicol. 38 (1) (2024) e23622.
[41] M. Li, X.-f. Lin, J. Lu, B.-r. Zhou, D. Luo, Hesperidin ameliorates UV radiation-induced skin damage by abrogation of oxidative stress and inflammatory in HaCaT cells, J. Photochem. Photobiol. B Biol. 165 (2016) 240–245.
[42] T. Wang, L. Guo, S. Wu, Y. Xu, J. Song, Y. Yang, H. Zhang, D. Li, Y. Li, X. Jiang, Polyphenolic platform ameliorated sanshool for skin Photoprotection, Adv. Sci. 2310012 (2024).
[43] Z. Zuo, S. He, Y. Qiu, R. Guo, Y. He, C. Jiao, Y. Xia, W. Liu, C. Luan, W. Guo, Salvianolic acid a prevents UV-induced skin damage by inhibiting the cGAS-STING pathway, Int. Immunopharmacol. 132 (2024) 111971.
[44] F. Yu, D. Gong, D. Yan, H. Wang, N. Witman, Y. Lu, W. Fu, Y. Fu, Enhanced adipose-derived stem cells with IGF-1-modified mRNA promote wound healing following corneal injury, Mol. Ther. 31 (8) (2023) 2454–2471.
[45] S. Cheng, R. Lv, J. Xu, A.R. Hirman, L. Du, IGF-1-expressing placenta-derived mesenchymal stem cells promote scalding wound healing, J. Surg. Res. 265 (2021) 100–113.
[46] S. Wu, G. Liu, P. Shao, X. Lin, J. Yu, H. Chen, H. Li, S. Feng, Transdermal Sustained Release Properties and Anti-Photoaging Efficacy of Liposome-Thermosensitive Hydrogel System (Adv. Healthcare Mater. 2/2024), Advanced Healthcare Materials 13(2) (2024) 2470008.
[47] T.S. Nagapan, W.N. Lim, A.R. Ghazali, D.F. Basri, Pterostilbene supplementation inhibits early inflammatory response and oxidative stress in UVB-induced BALB/C mice, Sains Malays 50 (2021) 1407–1414.
[48] P.N. Sudha, M.H. Rose, Beneficial effects of hyaluronic acid, Adv. Food Nutr. Res. 72 (2014) 137–176.
[49] M. Heatley, Ki67 protein: the immaculate deception? Histopathology 40 (5) (2002) 483.
[50] F. Unglaub, M.B. Wolf, A. Dragu, R.E. Horch, Molecular events of cellular apoptosis and proliferation in the early tendon healing period, J. Hand Surg. 35 (4) (2010) 691–692.
[51] M. Miodovnik, R. Koren, E. Ziv, A. Ravid, The inflammatory response of keratinocytes and its modulation by vitamin D: the role of MAPK signaling pathways, J. Cell. Physiol. 227 (5) (2012) 2175–2183.
[52] P. Xu, M. Zhang, X. Wang, Y. Yan, Y. Chen, W. Wu, L. Zhang, L. Zhang, Antioxidative effect of quetiapine on acute ultraviolet-B-induced skin and HaCaT cell damage, Int. J. Mol. Sci. 19 (4) (2018) 953.
[53] M.-J. Kwon, B. Kim, Y.S. Lee, T.-Y. Kim, Role of superoxide dismutase 3 in skin inflammation, J. Dermatol. Sci. 67 (2) (2012) 81–87.
[54] S.L. Marklund, E. Holme, L. Hellner, Superoxide dismutase in extracellular fluids, Clin. Chim. Acta 126 (1) (1982) 41–51.